Gravitational lensing in an exotic spacetime

Takao Kitamura

March 3, 2016

Abstract

The gravitational lensing effects in the weak gravitational field by exotic lenses have been investigated to probe non-luminous exotic objects. Gravitational lenses in a strong gravitational field also are important since they are one of tests for general relativity, black holes and exotic objects. For instance, it is known that the light rays passing just outside the photon sphere make faint images in the Schwarzschild spacetime and in wormhole spacetimes.

First, We examine a gravitational lens model inspired by modified gravity theories, exotic matter and energy. We study an asymptotically flat, static and spherically symmetric spacetime that is assumed in such a way that the spacetime metric depends on the inverse distance to the power of positive n in the weak field approximation. It is shown analytically and numerically that there is a lower limit on the source angular displacement from the lens object to get demagnification. Demagnifying gravitational lenses could appear, provided the source position β and the power n satisfy $\beta > 2/(n+1)$ in the units of the Einstein ring radius under a large n approximation. Unusually, the total amplification of the lensed images, though they are caused by the gravitational pull, could be less than the unity. Therefore, time-symmetric demagnification parts in numerical light curves by gravitational microlensing (Abe, Astrophys. J. 725, 787, 2010) may be an evidence of an Ellis wormhole (being an example of traversable wormholes) but they do not always prove it. Such a gravitational demagnification of the light might be used for hunting a clue of exotic matter and energy that are described by an equation of state more general than the Ellis wormhole case. Numerical calculations for $n = 3$ and 10 cases show maximally ~ 10 and ~ 60 percent depletion of the light, when the source position is $\beta \sim 1.1$ and $\beta \sim 0.7$, respectively.

Next, we consider gravitational lensing shear by the demagnifying lens models and other models such as negative-mass compact objects causing the gravitational repulsion on light rays like a concave lens. It is shown that images by the lens models for the gravitational pull are tangentially elongated, whereas those by the repulsive ones are radially distorted. This feature of lensed image shapes may be used for searching (or constraining)

localized exotic matter or energy with gravitational lensing surveys. It is suggested also that an underdense region such as a cosmic void might produce radially elongated images of background galaxies rather than tangential ones.

Next we consider microlensed image centroid motions by the exotic lens models. Numerical calculations show that, for large n cases in the convex-type models, the centroid shift from the source position might move on a multiply-connected curve like a bow tie, while it is known to move on an ellipse for $n = 1$ case and to move on an oval curve for $n = 2$. The distinctive feature of the microlensed image centroid may be used for searching (or constraining) localized exotic matter or energy with astrometric observations. It is shown also that the centroid shift trajectory for concave-type repulsive models might be elongated vertically to the source motion direction like a prolate spheroid, whereas that for convex-type models such as the Schwarzschild one is tangentially elongated like an oblate spheroid.

Finally, we investigate the gravitational lensing effects in the Tangherlini spacetime in the weak gravitational field and the strong field limit. The gravitational lens model in the Tangherlini spacetime would work as a wide-range toy model for exotic lens models with the photon sphere since it is the all-dimensional solution of the Einstein equation. We study the deflection angle of the light and the magnifications of images in the weak approximation and in the strong field limit. We derive the divergent part of the deflection angle in all dimensions and the regular part of the deflection angle in 4, 5 and 7 dimensions in the strong field limit, the deflection angle in all dimensions under the weak gravitational approximation and the relation between the size of the Einstein ring and the ones of the rings in the strong gravitational field. We also show that the images in the strong gravitational field are always fainter than the images in the weak gravitational field. We conclude that the images in the strong gravitational field have little effect on the total light curve and that the characteristic demagnification of the light curve will appear after considering the images in the strong gravitational field in higher dimensions. The gravitational lensing in the strong field limit in higher dimension would be related to the nature of the higher dimensional black hole.

Contents

Acknowledgements

I would like to express the deepest appreciation to supervisor professor Hideki Asada for continuously giving me a lot of useful advice, encouragement, and support over the years. I want to thank Yuuiti Sendouda for his comment, good advice, and support. I would like to thank Naoki Tsukamoto for his comment, and help in interpreting the significance of the results of our study.I would like to thank Fumio Abe for his comment, and help in interpreting the significance of the results of our study. I am deeply grateful to Masumi Kasai, Ryuichi Takahashi, and Nobusuke Takahashi for their help in a variety of contexts. I have had support and encouragement of Kei Yamada. I am also grateful to the member of theoretical astrophysics group at Hirosaki University, especially to Koji Izumi, Yukiharu Toki, Koki Nakajima, Chisaki Hagiwara, Toshiaki Ono, Asahi Ishihara, and Yusuke Suzuki for their cooperation. Finally, I am deeply thankful to all who have supported me.

Chapter 1

Introduction

The bending of light is among the first experimental confirmations of the theory of general relativity. As one of the important tools in modern astronomy and cosmology, the gravitational lensing is widely used for investigating extrasolar planets, dark matter and dark energy.

The light bending is also of theoretical importance, in particular for studying a null structure of a spacetime. A rigorous form of the bending angle plays an important role in understanding properly a strong gravitational field [1, 2, 4, 6, 3, 5, 8, 9]. For example, strong gravitational lensing in a Schwarzschild black hole was considered by Frittelli, Kling and Newman [1], by Virbhadra and Ellis [2] and more comprehensively by Virbhadra [4]; Virbhadra, Narasimha and Chitre [6] studied distinctive lensing features of naked singularities. Virbhadra and Ellis [3] and Virbhadra and Keeton [5] later described the strong gravitational lensing by naked singularities; DeAndrea and Alexander [7] discussed the lensing by naked singularities to test the cosmic censorship hypothesis; Eiroa, Romero and Torres [8] treated Reissner-Nordström black hole lensing; Perlick [9] discussed the lensing by a Barriola-Vilenkin monopole and also that by an Ellis wormhole.

One of peculiar features of general relativity is that the theory admits a nontrivial topology of a spacetime, for instance a wormhole. An Ellis wormhole is a particular example of the Morris-Thorne traversable wormhole class [10, 11, 12]. Furthermore, wormholes are inevitably related with violations of some energy conditions in physics [28]. For instance, dark energy is introduced to explain the observed accelerated expansion of the universe by means of an additional energy-momentum component in the right-hand side of the Einstein equation. Furthermore, the left-hand side of the Einstein equation, equivalently the Einstein-Hilbert action, could be modified in various ways (nonlinear curvature terms, higher dimensions, and so on) inspired by string theory, loop quantum gravity and so on. Because of the nonlinear nature of

gravity, modifications to one (or both) side of the Einstein equation might admit spacetimes significantly different from the standard Schwarzschild spacetime metric, even if the spacetime is assumed to be asymptotically flat, static and spherically symmetric. One example is an Ellis wormhole (being an example of traversable wormholes).

Many years ago, scattering problems in wormhole spacetimes were discussed (for instance, [13, 14]). Interestingly, the Ellis wormhole has a zero mass at the spatial infinity but it causes the light deflection [13, 14]. Moreover, the gravitational lensing by wormholes has been recently investigated as an observational probe of such an exotic spacetime [15, 16, 9, 17, 18, 19, 20, 21, 23]. Several forms of the deflection angle by the Ellis wormhole have been recently derived and often used [9, 17, 24, 25, 18, 19, 20]. A reason for such differences has been clarified by several authors [26, 27]. Especially among these study, According to numerical calculations by Abe [18] and Toki [19], time-symmetric demagnification parts in light curves could appear by gravitational microlensing effects of the Ellis wormhole, and The astrometric image centroid trajectory by the Ellis wormhole is different from the standard one by a spherical lensing object that is expressed by the Schwarzschild metric respectively. Is the time-symmetric demagnification or the anomalous shift of the image centroid an evidence for the Ellis wormhole? It is very interesting to address this question.

Small changes in gravitational lensing in modified gravity theories such as $f(R)$ and fourth-order gravity have been studied (e.g. [29, 30, 31, 32]). Furthermore, Horvath, Gergely, and Hobill [34] studied lensing effects with negative convergence by so-called tidal charges in the Dadhich et al. solution, where, for a brane world black hole, the tidal charge arises from tidal forces acting at the brane-bulk boundary [35]. A point is that negative convergence in this case does not require any exotic matter. It comes from the Weyl curvature in higher dimensions.

Inspired by a huge number of modified theories, this paper assumes, in a phenomenological sense, that an asymptotically flat, static and spherically symmetric modified spacetime could depend on the inverse distance to the power of positive n in the weak field approximation. The Schwarzschild spacetime and the Ellis wormhole correspond to $n = 1$ and $n = 2$, respectively. Note that Birkhoff's theorem could say that cases $n \neq 1$ might be non-vacuum, if the models were interpreted in the framework of the standard Einstein equation.

The slightly modified gravitational lensing in modified gravity theories such as a fourth order $f(R)$ gravity theory has attracted interests (e.g. [29, 30, 31]). It has been shown that the total magnification of the lensed images is stable and always larger than the unity against a small spherical perturbation

of the Schwarzschild lens [32]. This suggests that demagnifying gravitational lenses would need a significantly modified structure of the spacetime. In Chapter 2, We discuss demagnifying gravitational lenses due to significantly modified spacetimes referring to Kitamura et al.[36]

Kitamura et al. [36] have shown that demagnification could occur for $n > 1$ including the Ellis wormhole case ($n = 2$). They have also shown that time-symmetric demagnification parts might appear in light curves due to gravitational microlensing effects by such exotic models, where light curves are useful in microlensing observations in our galaxy. For cosmological situations, however, the Einstein ring size becomes so large and hence the typical time scale is so long that light curves cannot be observable in cosmology. On the other hand, the image separation angle becomes sufficiently large, so that it can be practically measured. By using the latest result in the Sloan Digital Sky Survey Quasar Lens Search, Takahashi and Asada have recently set the first upper bound on the cosmic abundances of Ellis wormholes and also negative-mass compact objects [37]. In theoretical physics, negative mass is a hypothetical concept of matter whose mass is of opposite sign to the mass of normal matter. Although possible negative mass ideas have been often discussed since the 19th century, there has been no evidence for them [38, 39, 40, 41]. The negative masses might attract each other to form a negative massive clump, so that such clumps could reside in cosmological voids (e.g. [42]). Gibbons and Kodama [43] have shown that curvature-regular asymptotically flat solitons with negative mass are contained in the Myers-Perry family, though the soliton solutions in the odd spacetime dimensions might not express real astrophysical objects. However, the information on the image separation angle is not sufficient for distinguishing exotic lens models. In Chapter 3, we study shapes of lensed images due to significantly modified spacetimes with negative convergence or negative mass referring Izumi et al.[44] We show that images by the lens models for the gravitational pull (like a convex lens in optics) are tangentially elongated, whereas those by the repulsive ones (like a concave lens) are radially distorted. This study might concern the strong (or weak) lensing surveys at the extra-galactic or cosmological distance.

And, in Chapter 4, we investigate microlensed image centroid motions by such exotic gravitational lens models. The image centroid position gives us an additional information, so that the parameter degeneracy existing in photometric microlensing can be partially broken. Here, we focus on the astrometric microlensing in our galaxy. Studies of centroid displacements of lensed images have been often done for the Schwarzschild lens [45, 46, 47, 48, 49, 50, 51, 52]. Virbhadra and Keeton [5] have investigated the centroid displacement for naked singularities by using the Janis-Newman-Winicour

solution. Toki et al. [19] have studied the centroid motion by Ellis wormhole. The main results of Chapter4 are: (1) For certain exotic lens models, the centroid shift from the source position might move on a multiply-connected curve like a *bow tie* for large n cases, while it is known to move on an ellipse for $n = 1$ case [45, 49] and to move on an oval curve for $n = 2$ [19]. (2)For concave-type repulsive lens models, the centroid displacement might move on a simply-connected curve but might be elongated vertically to the source velocity, while it is tangentially elongated for Schwarzschild case.

However, these Chapters 2-4 concentrated on the weak gravitational field and do not cover the gravitational lensing effects in the strong gravitational field.

About half a century ago, the images in the strong gravitational field were found by Darwin [61, 62]. Darwin pointed out the existence of the relativistic images which are a series of faint images lying just outside the photon sphere [61] in the Schwarzschild spacetime. The countably infinite relativistic images are generally formed in spherically symmetric static spacetimes [63, 64, 9]. The gravitational lensing in the strong gravitational field by various black holes and wormholes has been investigated eagerly in the recent decade (see [2, 5, 4, 65, 66] and references therein).

In Chapter 5, we investigate the gravitational lensing effects in the weak field approximation and in the strong field limit of the Tangherlini spacetime [67]. The Tangherlini lens model would work as a wide-range toy model for the exotic lens objects with strong gravitational field since the Tangherlini spacetime is a solution of the Einstein equations in all dimensions. The Tangherlini lens model is expected to show the general features of the gravitational lensing effects by exotic gravitational objects in both the weak and strong gravitational field.

The gravitational lens in the strong field limit is related to the other phenomena such as the quasi-normal modes of a black hole [68, 69] and the high-energy absorption cross section [70] which are caused by the nature of the null geodesic near the photon sphere. Thus, the investigation of gravitational lensing effects of the all-dimensional black hole in the strong field limit would give us a new perspective on the intrinsic property of the all-dimensional black hole.

In this paper we use the units in which the light speed $c = 1$ and Newton's constant $G = 1$.

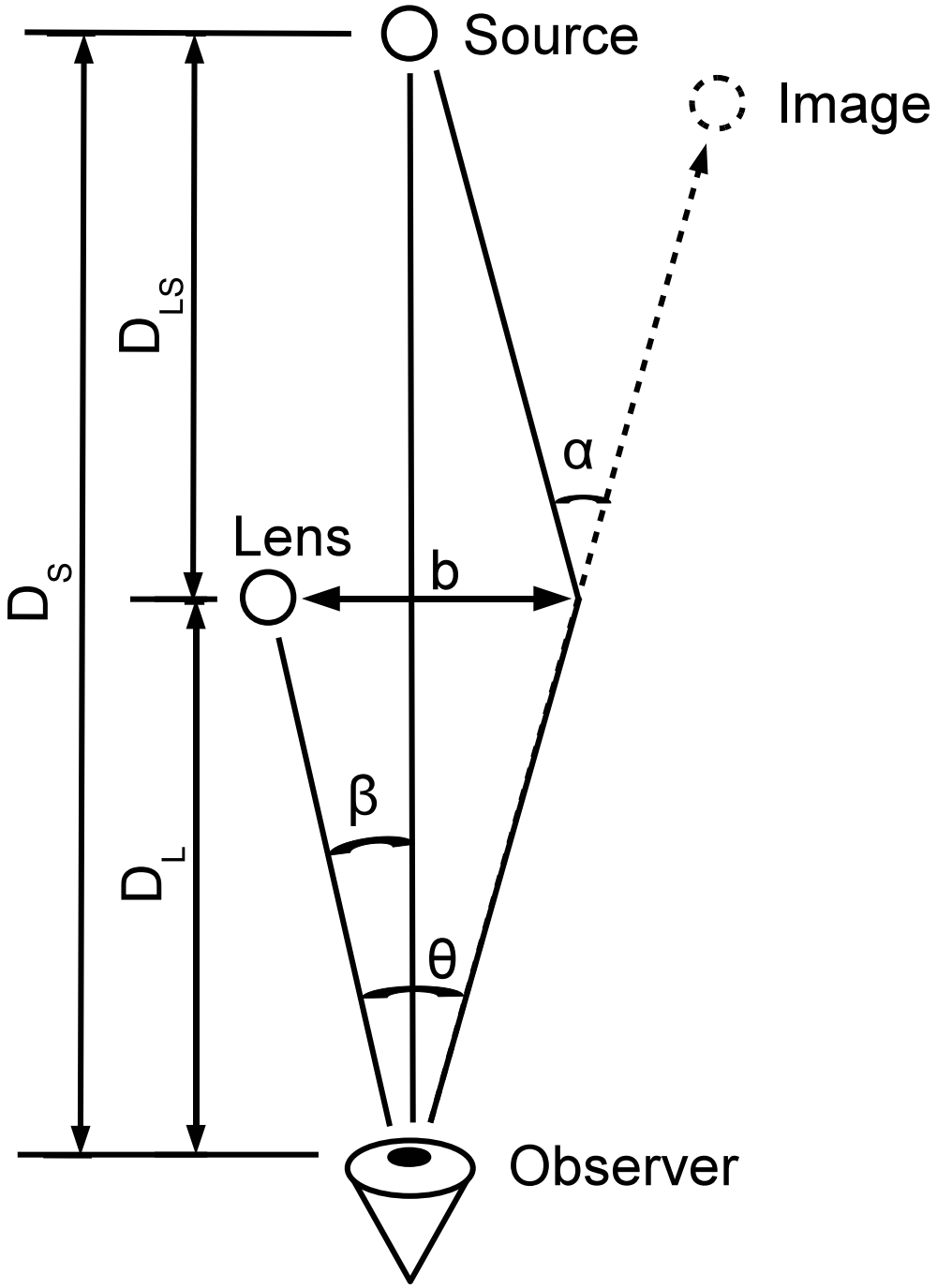

Figure 1.1: Source and image trajectories in the sky from the position of the observer.[19]

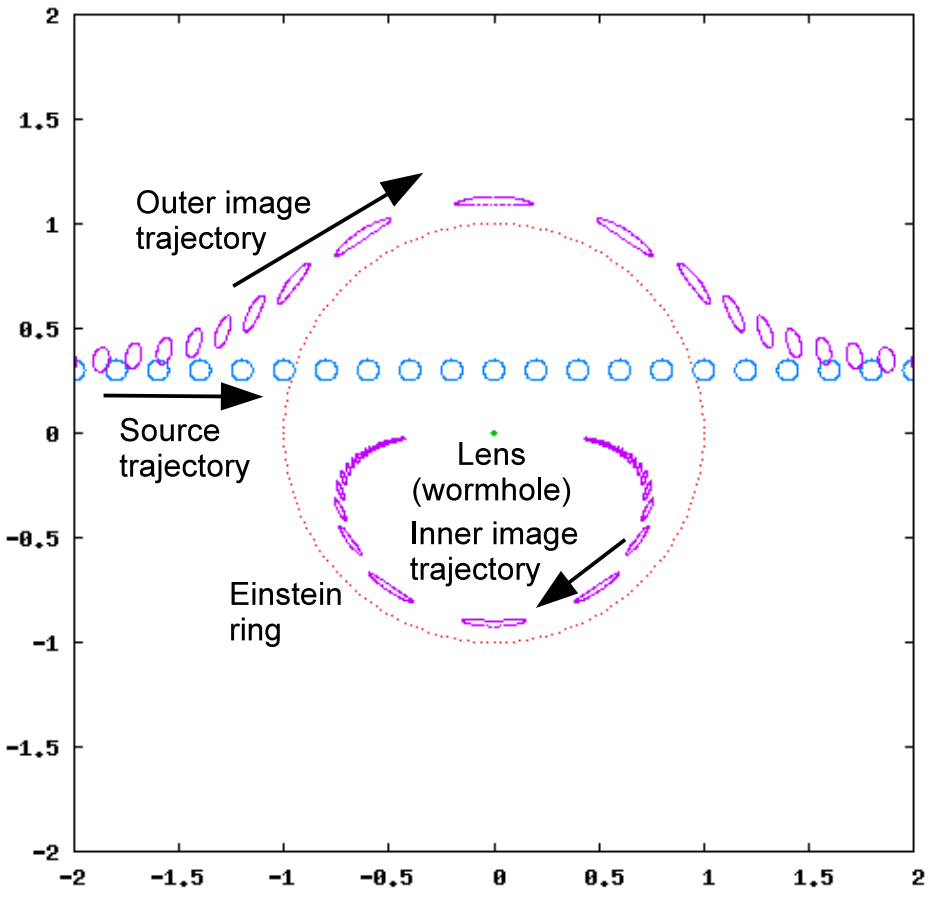

Figure 1.2: Source and image trajectories in the sky from the position of the observer.[19]

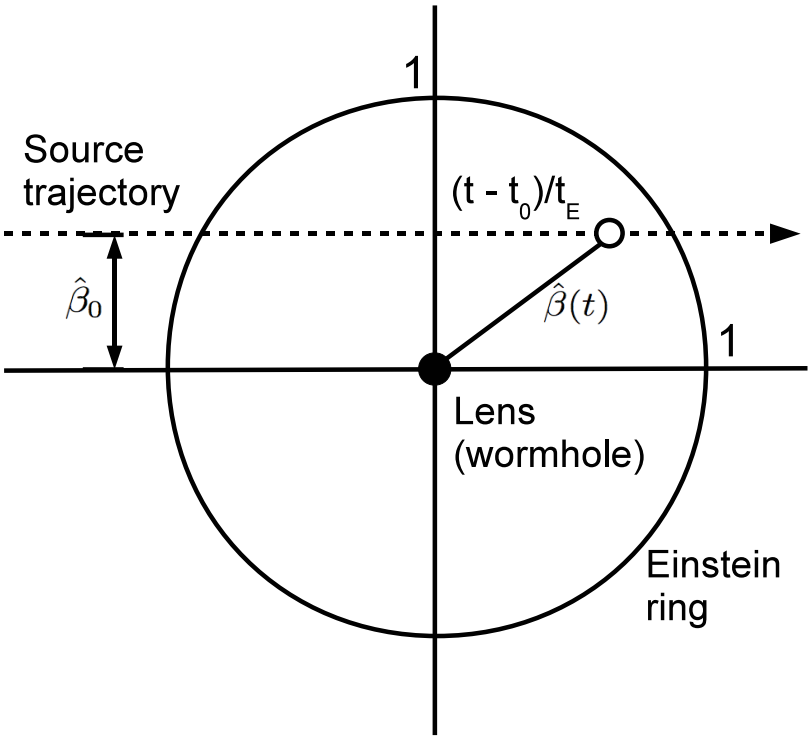

Figure 1.3: Sketch of the relation between the source trajectory and the lens (wormhole) in the sky. All quantities are normalized by the angular Einstein radius θ_E.[19]

Chapter 2

Gravitational microlensing by modified spacetime

2.1 The modified spacetime model and deflection angle

Magnification of the apparent brightness of a distant star by the gravitational lensing effect of another star was predicted by [83]. This kind of lensing effect is called "microlensing" because the images produced by the gravitational lensing are very close to each other and are difficult for the observer to resolve. The brightness changing effect was discovered in 1993 [77, 78, 82] and has been used to detect astronomical objects that do not emit observable signals (such as visible light, radio waves, and X rays) or are too faint to observe. Microlensing has successfully been applied to detect extrasolar planets [85, 84] and brown dwarfs [86, 91]. Microlensing is also used to search for unseen black holes [81, 87, 90] and massive compact halo objects [80, 89, 88], a candidate for dark matter.

This paper assumes that an asymptotically flat, static and spherically symmetric modified spacetime could depend on the inverse distance to the power of positive n in the weak field approximation. We consider the light propagating through a four-dimensional spacetime, though the whole spacetime may be higher dimensional. The four-dimensional spacetime metric is expressed as

$$ds^2 = -\left(1-\frac{\varepsilon_1}{r^n}\right)dt^2 + \left(1+\frac{\varepsilon_2}{r^n}\right)dr^2 + r^2(d\theta^2+\sin^2\theta d\phi^2) + O(\varepsilon_1^2,\varepsilon_2^2,\varepsilon_1\varepsilon_2), \tag{2.1}$$

where r is the circumference radius and ε_1 and ε_2 are small book-keeping parameters in the following iterative calculations. Here, ε_1 and ε_2 may be either

positive or negative, respectively. Negative ε_1 and ε_2 for $n = 1$ correspond to a negative mass (in the linearized Schwarzschild metric).

For investigating the light propagation, it is useful below to make a conformal transformation with a factor as $(1-\varepsilon_1/r^n)^{1/2}$. The null structure such as the light propagation is not affected by the conformal transformation. At the linear order of ε_1 and ε_2, the spacetime metric takes a simpler form as

$$d\bar{s}^2 = -dt^2 + \left(1 + \frac{\varepsilon}{R^n}\right) dR^2 + R^2(d\theta^2 + \sin^2\theta d\phi^2) + O(\varepsilon^2), \tag{2.2}$$

where $\varepsilon \equiv n\varepsilon_1 + \varepsilon_2$ and

$$R^2 \equiv \frac{r^2}{\left(1 - \frac{\varepsilon_1}{r^n}\right)}. \tag{2.3}$$

Note that the only one parameter ε enters the conformally transformed metric.

For this metric, one can find the Lagrangian for a massless particle. Without loss of generality, we focus on the equatorial plane $\theta = \pi/2$, since the spacetime is spherically symmetric. By using the constants of motion associated with the timelike and rotational Killing vectors, the deflection angle of light is calculated at the linear order as

$$\begin{aligned} \alpha &= 2\int_{R_0}^{\infty} \frac{d\phi(R)}{dR} dR - \pi \\ &= \frac{\varepsilon}{b^n} \int_0^{\frac{\pi}{2}} \cos^n\psi d\psi + O(\varepsilon^2), \end{aligned} \tag{2.4}$$

where R_0 and b denote the closest approach and the impact parameter of the light ray, respectively. This deflection angle recovers the Schwarzschild ($n = 1$) and Ellis wormhole ($n = 2$) cases. For particular cases, the above (always positive) integral factor becomes

$$\begin{aligned} \int_0^{\frac{\pi}{2}} \cos^n\psi d\psi &= \frac{(n-1)!!}{n!!}\frac{\pi}{2} \quad (\text{even } n), \\ &= \frac{(n-1)!!}{n!!} \quad (\text{odd } n), \\ &= \frac{\sqrt{\pi}}{2}\frac{\Gamma\left(\frac{n+1}{2}\right)}{\Gamma\left(\frac{n+2}{2}\right)} \quad (\text{real } n > 0), \end{aligned} \tag{2.5}$$

Henceforth, the deflection angle is denoted simply as $\alpha(b) = \bar{\varepsilon}/b^n$ by absorbing the numerical constant into $\bar{\varepsilon}$ parameter.

2.2 Modified lens equation and its solutions

Under the thin lens approximation, we consider the lens configuration which is given in Figure 1.1,1.3. It is useful to consider the lens equation as [33]

$$\beta = \frac{b}{D_L} - \frac{D_{LS}}{D_S}\alpha(b), \tag{2.6}$$

where β denotes the angular position of the source and D_L, D_S, D_{LS} are the distances from the observer to the lens, from the observer to the source, and from the lens to the source, respectively. We wish to consider significant magnification (or demagnification), which could occur for a source in (or near) the Einstein ring. The Einstein ring is defined for $\beta = 0$ [33]. If $\varepsilon < 0$, Eq. (2.6) has no positive roots for $\beta = 0$, because of the repulsive force in the particular gravity model. For $\varepsilon > 0$, on the other hand, there is always a positive root corresponding to the Einstein ring. The negative ε case has of less astronomical relevance. Therefore, let us consider the positive ε case (causing the gravitational pull) in the following.

In the units of the Einstein ring radius, Eq. (2.6) is rewritten as

$$\hat{\beta} = \hat{\theta} - \frac{1}{\hat{\theta}^n} \quad (\hat{\theta} > 0), \tag{2.7}$$

$$\hat{\beta} = \hat{\theta} + \frac{1}{(-\hat{\theta})^n} \quad (\hat{\theta} < 0), \tag{2.8}$$

where $\hat{\beta} \equiv \beta/\theta_E$ and $\hat{\theta} \equiv \theta/\theta_E$ for the angular position of the image $\theta \equiv b/D_L$.

Let us consider two lines defined by $Y = 1/\hat{\theta}^n$ and $Y = \hat{\theta} - \beta$ in the $\hat{\theta} - Y$ plane. For $\hat{\theta} > 0$, therefore, we have the only one intersection of the two lines that is corresponding to one image position. Similarly, the only one image appears for $\hat{\theta} < 0$.

For a general positive n (e.g. $n = 5$), it is impossible to find the exact solutions for the modified lens equation. For clarifying parameter dependence, we employ analytic but approximate methods rather than numerical calculations. In astronomy, furthermore, only the significantly amplified images become detectable in gravitational microlensing. Such events occur only when a source such as a distant star crosses the Einstein ring. We thus focus on such an Einstein ring-crossing case as $\hat{\beta} < 1$ in the units of the Einstein ring, for which Eqs. (2.7) and (2.8) are solved in the Taylor series form with

respect to $\hat{\beta}$. We obtain

$$\hat{\theta}_+ = 1 + \frac{1}{n+1}\hat{\beta} + \frac{1}{2}\frac{n}{(n+1)^2}\hat{\beta}^2 + O(\hat{\beta}^3) \quad (\hat{\theta} > 0), \tag{2.9}$$

$$\hat{\theta}_- = -1 + \frac{1}{n+1}\hat{\beta} - \frac{1}{2}\frac{n}{(n+1)^2}\hat{\beta}^2 + O(\hat{\beta}^3) \quad (\hat{\theta} < 0), \tag{2.10}$$

2.3 Demagnification condition

The amplification factor denoted as A is $|(\beta/\theta)(d\beta/d\theta)|^{-1}$, namely the inverse Jacobian of the gravitational lens mapping between the source and image position vectors [33]. By using Eqs. (2.9) and (2.10), the amplification factor of each image which is denoted by A_+ and A_-, respectively becomes

$$A_\pm = \frac{1}{\hat{\beta}(n+1)} + O(\hat{\beta}^0), \tag{2.11}$$

where a difference between A_+ and A_- appears at the next order in $\hat{\beta}$. The total amplification is thus

$$\begin{aligned} A_{tot} &\equiv A_+ + A_- \\ &= \frac{2}{\hat{\beta}(n+1)} + O(\hat{\beta}^0), \end{aligned} \tag{2.12}$$

For the Schwarzschild case ($n = 1$), $A_{tot} = 1/\hat{\beta}$. This is always larger than the unity for $\hat{\beta} < 1$, in concordance with the well-known fact. Demagnification of the total lensed images could occur, however, if

$$\hat{\beta} > \frac{2}{n+1}. \tag{2.13}$$

The larger the power n, the more likely the demagnification. One might guess that demagnification could be caused for a smaller $\hat{\beta}$, especially $\hat{\beta} = 0$. However, this is not the case. Eq. (2.13) suggests that the total demagnification could occur, only when $\hat{\beta}$ is small but larger than the critical value $2/(n+1)$ under a large n approximation. Note that compatibility of the assumption $\hat{\beta} < 1$ and Eq. (2.13) implies $n > 1$. Namely, Eq. (2.13) becomes a better approximation as n is larger than the unity.

The above argument is based on the near zone approximation ($\hat{\beta} < 1$). For a test of the analytic result, we perform numerical calculations. We consider $n = 10$, which might be one of higher dimensional models inspired by string theory. Eq. (2.13) suggests that demagnification of the total lensed

images could occur only for $\hat{\beta} > 2/11 = 0.182$. Figure 2.1 shows numerical results for $n = 1, 2, 3$ and 10.

In the case of $n = 10$,

the analytic result for the critical value as $\hat{\beta} = 2/11 = 0.182$ is in good agreement with the numerical one $\hat{\beta} = 0.187$.

Figure 2.2 shows numerical light curves for $n = 1, 2, 3, 10$. As the power n is larger, time-symmetric demagnification parts in the light curves become longer in time and larger in depth. Cases of $n = 3$ and 10 show maximally ~ 10 and ~ 60 percent depletion of the light,

when the source position is $\hat{\beta} \sim 1.1$ and $\hat{\beta} \sim 0.7$, respectively.

Before closing this section, we briefly mention an effective mass. A simple application of the standard lens theory [33] suggests that the deflection ($\alpha = \bar{\varepsilon}/b^n$) and magnification studied here correspond to a convergence (scaled surface mass density) of the form as

$$\kappa(b) = \frac{\bar{\varepsilon}(1-n)}{2}\frac{1}{b^{n+1}}. \tag{2.14}$$

For $n > 1$, therefore, the effective surface mass density of the lens object is interpreted as negative in the framework of the standard lens theory. This means that the matter (and energy) need to be exotic if $n > 1$.

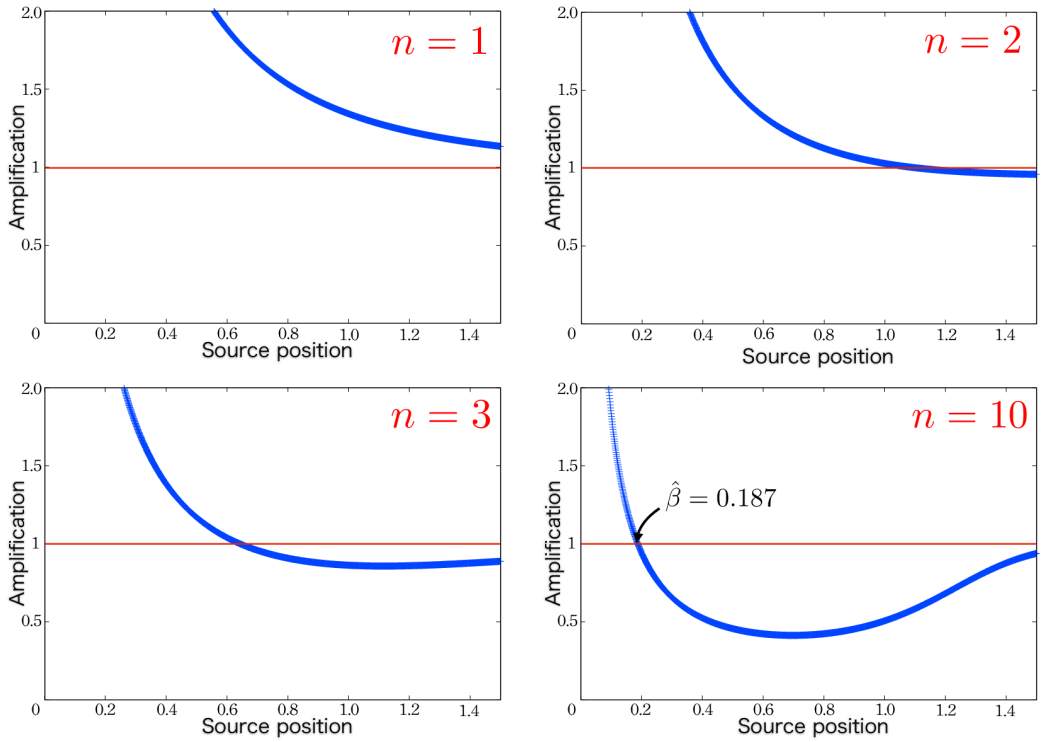

Figure 2.1: Total amplification factor of the lensed images as a function of the source position $\hat{\beta}$ for $n = 1, 2, 3$ and 10. Top left, top right, bottom left and bottom right panels are corresponding to $n = 1, 2, 3$ and 10, respectively. In the case of $n = 10$, the total amplification factor is larger than the unity for $\hat{\beta} < 0.187$, whereas it is smaller for $\hat{\beta} > 0.187$. For convenience, a thin (red in colors) line denotes $A_{tot} = 1$. [36]

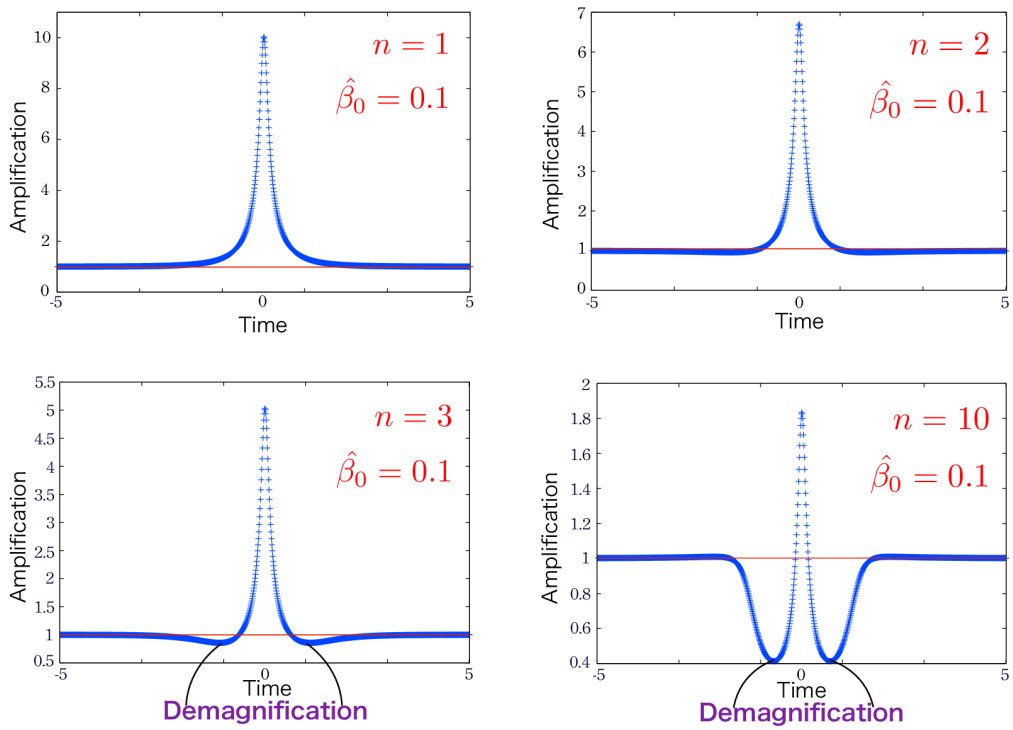

Figure 2.2: Numerical light curves for the same minimum impact parameter of the light trajectory $\hat{\beta}_0 = 0.1$. The source star moves at constant speed and the source position changes as $\hat{\beta}(t) = (\hat{\beta}_0^2 + t^2)^{1/2}$, where time is normalized by the Einstein ring radius crossing time. Top left, top right, bottom left and bottom right panels are corresponding to $n = 1, 2, 3$ and 10, respectively. For convenience, a thin (red in colors) line denotes $A_{tot} = 1$. [36]

2.4 Summary of this chapter

We examined a gravitational lens model inspired by modified gravity theories, exotic matter and energy. By using an asymptotically flat, static and spherically symmetric spacetime model of which metric depends on the inverse distance to the power of positive n, it was shown in the weak field and thin lens approximations that demagnifying gravitational lenses could appear, provided the impact parameter of light $\hat{\beta}$ and the power n satisfy $\hat{\beta} > 2/(n+1)$ in the units of the Einstein ring radius under a large n approximation.

Therefore, time-symmetric demagnification parts in numerical light curves by gravitational microlensing (Abe, Astrophys. J. 725, 787, 2010) may be an evidence of an Ellis wormhole but they do not always prove it. Such a gravitational demagnification of the light might be used for hunting a clue of exotic matter and energy that are described by an equation of state more general than the Ellis wormhole case. Examples of $n = 3$ and 10 show maximally ~ 10 and ~ 60 percent depletion of the light, when the source position is $\hat{\beta} \sim 1.1$ and $\hat{\beta} \sim 0.7$, respectively.

It is left as a future work to perform a numerical campaign for the vast parameter space.

The above gravitational demagnification of light occurs, presumably because modified lenses could act as an effectively negative (quasi-local) mass on a particular light ray (through the Ricci focusing). Regarding this issue, a more rigorous formulation is needed. It would be interesting to study a relation between the model parameter n and vital modified gravity theories (or matter models with an exotic equation of state) and also to make an interpretation of the parameter n in the framework of the theory of general relativity.

The analytical approximate solution in this paper is obtained at the linear order of $1/\hat{\beta}$ to discuss the total magnification. Tsukamoto and Harada [21] have studied the next order of $1/\hat{\beta}$ to discuss the signed magnification sums, namely the difference between the amplifications of two images.

Chapter 3

Gravitational lensing shear by modified spacetime

3.1 Modified spacetime model and modified lens equation

3.1.1 Modified bending angle of light

Following Kitamura et al. [36], the present chapter assumes that an asymptotically flat, static and spherically symmetric modified spacetime could depend on the inverse distance to the power of positive n in the weak field approximation. Note that some of the notations are different from those in Chapter 2. We consider the light propagation through a four-dimensional spacetime, though the whole spacetime may be higher dimensional. The four-dimensional spacetime metric is expressed as

$$ds^2 = -\left(1 - \frac{\varepsilon_1}{r^n}\right) dt^2 + \left(1 + \frac{\varepsilon_2}{r^n}\right) dr^2 + r^2(d\Theta^2 + \sin^2\Theta d\phi^2) + O(\varepsilon_1^2, \varepsilon_2^2, \varepsilon_1\varepsilon_2), \tag{3.1}$$

where r is the circumference radius and ε_1 and ε_2 are small book-keeping parameters in the following iterative calculations. Here, ε_1 and ε_2 may be either positive or negative, respectively. Negative ε_1 and ε_2 for $n = 1$ correspond to a negative mass (in the linearized Schwarzschild metric).

Without loss of generality, we focus on the equatorial plane $\Theta = \pi/2$, since the spacetime is spherically symmetric. The deflection angle of light is obtained at the linear order as [36]

$$\alpha = \frac{\varepsilon}{b^n} \int_0^{\frac{\pi}{2}} \cos^n \psi d\psi + O(\varepsilon^2), \tag{3.2}$$

where the integral is positive definite, b denotes the impact parameter of the light ray, and we define $\varepsilon \equiv n\varepsilon_1 + \varepsilon_2$. By absorbing the positive integral into the parameter ε, we rewrite the linear-order deflection angle simply as $\alpha = \bar{\varepsilon}/b^n$, where the sign of $\bar{\varepsilon}$ is the same as that of ε. This deflection angle recovers the Schwarzschild ($n = 1$) and Ellis wormhole ($n = 2$) cases. For $\varepsilon > 0$, the deflection angle of light is always positive, which means that the corresponding spacetime model causes the gravitational pull on light rays. For $\varepsilon < 0$, on the other hand, it is inevitably negative, which implies the gravitational repulsion on light rays like a concave lens. Tsukamoto and Harada [21] employ as an *ansatz* the same modified bending angle as what is derived from the spacetime metric by Kitamura et al. [36].

We mention an effective mass. A simple application of the standard lens theory [33] suggests that the deflection angle of light in the form of $\alpha = \bar{\varepsilon}/b^n$ corresponds to a convergence (scaled surface mass density) as

$$\kappa(b) = \frac{\bar{\varepsilon}(1-n)}{2}\frac{1}{b^{n+1}}. \tag{3.3}$$

For the weak-field Schwarzschild case ($n = 1$), it follows that the convergence vanishes. For $\varepsilon > 0$ and $n > 1$, the effective surface mass density of the lens object is interpreted as negative in the framework of the standard lens theory [36]. This means that the matter (and energy) need to be exotic if $\varepsilon > 0$ and $n > 1$. Also when $\varepsilon < 0$ and $n < 1$, the convergence is negative and hence the matter (and energy) need to be exotic. Interestingly, when $\varepsilon < 0$ and $n > 1$, the convergence is positive everywhere except for the central singularity and hence exotic matter (and energy) are not required in the framework of the standard lens theory, in spite of the gravitational repulsion on light rays. Attraction ($\varepsilon > 0$) and repulsion ($\varepsilon < 0$) in the above models do not have a one-to-one correspondence to positive convergence $\kappa > 0$ and negative one $\kappa < 0$. This point is summarized in Table 3.1.

3.1.2 Modified lens equation

Under the thin lens approximation, we consider the lens configuration which is given in Figure 1.1,1.3, it is useful to consider the lens equation as [33]

$$\beta = \frac{b}{D_{\rm L}} - \frac{D_{\rm LS}}{D_{\rm S}}\alpha(b), \tag{3.4}$$

where β denotes the angular position of the source and D_L, D_S, D_{LS} are the distances from the observer to the lens, from the observer to the source, and from the lens to the source, respectively.

For $\varepsilon > 0$, there is always a positive root corresponding to the Einstein ring for $\beta = 0$. The Einstein ring radius is defined as [33]

$$\theta_{\rm E} \equiv \left(\frac{\bar{\varepsilon} D_{\rm LS}}{D_{\rm S} D_{\rm L}^n} \right)^{\frac{1}{n+1}}. \tag{3.5}$$

If $\varepsilon < 0$, on the other hand, Eq. (3.4) has no positive root for $\beta = 0$. This is because this case describes the repulsive force. For later convenience in normalizing the lens equation, we define the (tentative) Einstein ring radius for $\varepsilon < 0$ as

$$\theta_{\rm E} \equiv \left(\frac{|\bar{\varepsilon}| D_{\rm LS}}{D_{\rm S} D_{\rm L}^n} \right)^{\frac{1}{n+1}}, \tag{3.6}$$

though the Einstein ring does not appear for this case. This radius gives a typical angular size for $\varepsilon < 0$ lenses.

3.2 Gravitational lensing shear

3.2.1 $\varepsilon > 0$ case

Let us begin with a $\varepsilon > 0$ case. As already stated, the matter (and energy) need to be exotic if $n > 1$. In the units of the Einstein ring radius, Eq. (3.4) is rewritten in the vectorial form as

$$\hat{\boldsymbol{\beta}} = \hat{\boldsymbol{\theta}} - \frac{\hat{\boldsymbol{\theta}}}{\hat{\theta}^{n+1}} \quad (\hat{\theta} > 0), \tag{3.7}$$

$$\hat{\boldsymbol{\beta}} = \hat{\boldsymbol{\theta}} - \frac{\hat{\boldsymbol{\theta}}}{(-\hat{\theta})^{n+1}} \quad (\hat{\theta} < 0), \tag{3.8}$$

where we normalize $\hat{\beta} \equiv \beta/\theta_E$ and $\hat{\theta} \equiv \theta/\theta_E$ for the angular position of the image $\theta \equiv b/D_L$, and $\hat{\boldsymbol{\beta}}$ and $\hat{\boldsymbol{\theta}}$ denote the corresponding vectors. There is always one image for $\hat{\theta} > 0$, while the other image appears for $\hat{\theta} < 0$ [36].

Let us study the lensing shear that is generally defined via the magnification matrix $A_{ij} \equiv \partial\beta^i/\partial\theta_j$ [33]. After straightforward computations, the magnification matrix for $\hat{\theta} > 0$ becomes explicitly

$$(A_{ij}) = \begin{pmatrix} 1 - \dfrac{1}{\hat{\theta}^{n+1}} + (n+1)\dfrac{\hat{\theta}_x \hat{\theta}_x}{\hat{\theta}^{n+3}} & (n+1)\dfrac{\hat{\theta}_x \hat{\theta}_y}{\hat{\theta}^{n+3}} \\ (n+1)\dfrac{\hat{\theta}_x \hat{\theta}_y}{\hat{\theta}^{n+3}} & 1 - \dfrac{1}{\hat{\theta}^{n+1}} + (n+1)\dfrac{\hat{\theta}_y \hat{\theta}_y}{\hat{\theta}^{n+3}} \end{pmatrix}. \tag{3.9}$$

It is diagonalized by using its eigen values $\lambda_\pm$ as

$$\begin{aligned}(A_{ij}) &= \begin{pmatrix} 1-\kappa-\gamma & 0 \\ 0 & 1-\kappa+\gamma \end{pmatrix} \\ &\equiv \begin{pmatrix} \lambda_- & 0 \\ 0 & \lambda_+ \end{pmatrix}, \end{aligned} \tag{3.10}$$

where the x and y coordinates are chosen along the radial and tangential directions, respectively, such that $(\hat{\theta}_i) = (\hat{\theta}, 0)$ and $(\hat{\beta}_i) = (\hat{\beta}, 0)$. Hence, the radial elongation factor is $1/\lambda_-$, while the tangential one is $1/\lambda_+$.

First, let us investigate the primary image ($\hat{\theta} > 0$). By using Eq. (3.7), we obtain

$$\lambda_+ = \frac{\hat{\beta}}{\hat{\theta}} = 1 - \frac{1}{\hat{\theta}^{n+1}}, \tag{3.11}$$

$$\lambda_- = \frac{d\hat{\beta}}{d\hat{\theta}} = 1 + \frac{n}{\hat{\theta}^{n+1}}. \tag{3.12}$$

To reach Eqs. (3.11) and (3.12), we need several steps, where first the Jacobian matrix is computed and next the matrix is diagonalized. Note that, for our axially symmetric cases, there is a shortcut of deriving Eqs. (3.11) and (3.12) without doing such lengthy calculations. In the shortcut, one may start with the x and y coordinates that are locally chosen along the radial and tangential directions, respectively, such that $(\hat{\theta}_i) = (\hat{\theta}, 0)$ and $(\hat{\beta}_i) = (\hat{\beta}, 0)$. Then, infinitesimal changes in $\hat{\boldsymbol{\beta}}$ and $\hat{\boldsymbol{\theta}}$ can be written as $(d\hat{\theta}_i) = (d\hat{\theta}, \hat{\theta} d\phi)$ and $(d\hat{\beta}_i) = (d\hat{\beta}, \hat{\beta} d\phi)$, where ϕ denotes the azimuthal angle. The axial symmetry allows that $\hat{\theta}$ and $\hat{\beta}$ are independent of ϕ, which means that the off-diagonal terms vanish in the local coordinates. Hence, one can immediately obtain Eqs. (3.11) and (3.12) [93].

If and only if $n > -1$, one can show $\lambda_- > \lambda_+$. Therefore, the primary image is always tangentially elongated. See also Figure 3.1 for κ and $\lambda_\pm$ that are numerically calculated for $n = 0.5$, 1, 2 and 3. For these four cases, λ_- is always larger than λ_+. The convergence κ is positive for $n = 0.5$, while it is negative for $n = 2$ and 3. It follows that $n = 1$ corresponding to the Schwarzschild lens leads to $\kappa = 0$.

Eqs. (3.11) and (3.12) give the convergence and the shear as

$$\begin{aligned}\kappa &= 1 - \frac{\lambda_+ + \lambda_-}{2} \\ &= \frac{1-n}{2} \frac{1}{\hat{\theta}^{n+1}}, \end{aligned} \tag{3.13}$$

$$\gamma = \frac{\lambda_+ - \lambda_-}{2} = -\frac{1+n}{2}\frac{1}{\hat{\theta}^{n+1}}, \tag{3.14}$$

respectively. It follows that this result of κ agrees with Eq. (3.3).

Next, we study the secondary image ($\hat{\theta} < 0$). By using Eq. (3.8), one can show $\lambda_- > \lambda_+$, if and only if $n > -1$. Hence, the secondary image also is tangentially elongated. See also Figure 3.2 for $\varepsilon > 0$ and $n = 2$, where one can see a pair of tangential images.

Finally, we mention the dependence on the exponent n. A significantly elongated case such as a giant arc appears near the Einstein ring ($\hat{\theta} \sim 1$), around which Eqs. (3.11) and (3.12) are expanded as

$$\lambda_+ = (n+1)(\hat{\theta}-1) - \frac{(n+1)(n+2)}{2}(\hat{\theta}-1)^2 + O\left((\hat{\theta}-1)^3\right), \tag{3.15}$$

$$\lambda_- = n+1-n(n+1)(\hat{\theta}-1) + O\left((\hat{\theta}-1)^2\right). \tag{3.16}$$

where we used the identity $\hat{\theta} = 1 + (\hat{\theta} - 1)$. The ratio of the tangential elongation to the radial one (corresponding to the arc shape) is

$$\frac{\lambda_-}{\lambda_+} = \frac{1}{\hat{\theta}-1} + \left(1 - \frac{n}{2}\right) + O(\hat{\theta}-1). \tag{3.17}$$

This suggests that, for the fixed observed lens position $\hat{\theta}$, elongation of images becomes weaker, when n becomes larger. This dependence on n is true of also the secondary image.

3.2.2 $\varepsilon < 0$ case

Let us study $\varepsilon < 0$ case. In the units of the Einstein ring radius, Eq. (3.4) is rewritten in the vectorial form as

$$\hat{\boldsymbol{\beta}} = \hat{\boldsymbol{\theta}} + \frac{\hat{\boldsymbol{\theta}}}{\hat{\theta}^{n+1}} \quad (\hat{\theta} > 0), \tag{3.18}$$

$$\hat{\boldsymbol{\beta}} = \hat{\boldsymbol{\theta}} + \frac{\hat{\boldsymbol{\theta}}}{(-\hat{\theta})^{n+1}} \quad (\hat{\theta} < 0). \tag{3.19}$$

Without loss of generality, we assume $\hat{\beta} > 0$. Then, Eq. (3.19) has no root satisfying $\hat{\theta} < 0$, while Eq. (3.18) has at most two positive roots. Figure 3.3 shows that there are three cases of the image number. For a large impact parameter case, two images appear on the same side with respect to the lens

position, while no image appears for a small impact parameter. The only one image appears only when the impact parameter takes a particular value. Let us focus on the two image cases, from which the single image case can be discussed in the limit as the impact parameter approaches the particular value.

By using Eq. (3.18), we obtain

$$\lambda_+ = \frac{\hat{\beta}}{\hat{\theta}} = 1 + \frac{1}{\hat{\theta}^{n+1}}, \tag{3.20}$$

$$\lambda_- = \frac{d\hat{\beta}}{d\hat{\theta}} = 1 - \frac{n}{\hat{\theta}^{n+1}}. \tag{3.21}$$

One can show that $\lambda_- < \lambda_+$, if and only if $n > -1$. Hence, both images are everywhere radially elongated. See also Figure 3.4 for κ and $\lambda_\pm$ that are numerically calculated for $n = 0.5$, 1, 2 and 3. For these four cases, λ_+ is always larger than λ_-. The convergence κ is negative for $n = 0.5$, while it is positive for $n = 2$ and 3. It follows that $n = 1$ corresponding to the (negative-mass) Schwarzschild lens leads to $\kappa = 0$.

Eqs. (3.20) and (3.21) give the shear as

$$\begin{aligned} \gamma &= \frac{\lambda_+ - \lambda_-}{2} \\ &= \frac{1+n}{2}\frac{1}{\hat{\theta}^{n+1}}. \end{aligned} \tag{3.22}$$

A repulsive case might correspond to the lensing by a void-like mass distribution. The above calculations assume the flat (Minkowskian) background spacetime. If one wish to consider cosmological situations, the gravitational potential and the mass density might correspond to the scalar perturbation and the density contrast in the cosmological perturbation approach based on the Friedmann-Lemaitre background spacetime [33]. In this cosmological counterpart, the present model with $\kappa < 0$ might correspond to an underdense region called a cosmic void, in which the local mass density is below the cosmic mean density and the density contrast is thus negative. The gravitational force on the light rays by the surrounding region could be interpreted as repulsive ($\varepsilon < 0$), because the bending angle of light with respect to the center of the spherical void might be negative. Therefore, cosmic voids might correspond to a $\kappa < 0$ and $\varepsilon < 0$ case. Note that the positive convergence due to the cosmic mean density is taken into account in the definition of the cosmological distances. There are very few galaxies in voids compared with

in a cluster of galaxies. Hence, it is difficult to investigate gravity inside a void by using galaxies as a tracer. Gravitational lensing shear measurements would be another tool for studying voids.

Before closing this section, we mention whether we can distinguish radial elongation and tangential one in observations without knowing the lens position. Usually, lens objects cannot be directly seen except for visible lens objects such as galaxies. In particular, exotic lens models that are discussed in this paper might be invisible. In the above calculations, the origin of the two-dimensional coordinates is chosen as the center of the lens object, so that the radial and tangential directions can be well defined. For a pair of radially elongated images ($\varepsilon < 0$), they are in alignment with each other. For a pair of tangentially elongated images ($\varepsilon > 0$), they are parallel with each other. Therefore, one can distinguish radial elongation from tangential one by measuring such an image alignment in observations. See also Figure 3.2 for $\varepsilon < 0$ and $n = 2$, where one can see a pair of radial images.

3.3 Summary of this chapter

We examined gravitational lens models inspired by modified gravity theories, exotic matter and energy. By using an asymptotically flat, static and spherically symmetric spacetime model of which metric depends on the inverse distance to the power of positive n, it was shown in the weak field and thin lens approximations that images due to lens models for the gravitational pull on light rays are tangentially elongated, whereas those by the other models for the gravitational repulsion on light rays are always radially distorted.

As a cosmological implication, it is suggested that cosmic voids might correspond to a $\kappa < 0$ and $\varepsilon < 0$ case and hence they could produce radially elongated images rather than tangential ones. It would be interesting to investigate numerically light propagation through realistic voids in cosmological simulations, because the present model obeys a simple power-law. It is left for future work.

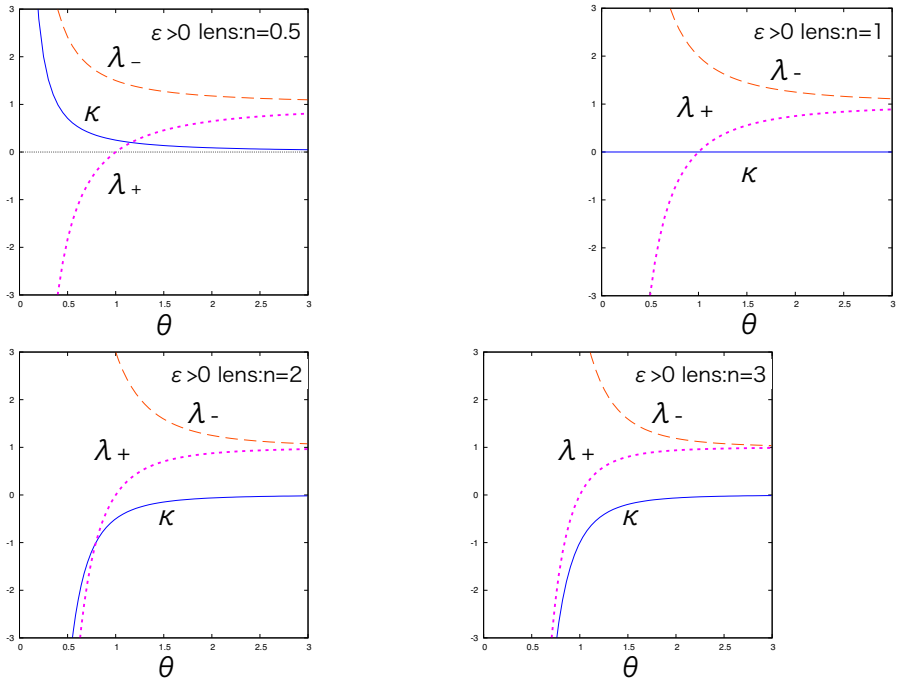

Figure 3.1: κ, λ_+ and λ_- for $\varepsilon > 0$. They are denoted by solid (blue in colors), dotted (purple in colors) and dashed (red in colors) curves, respectively. The horizontal axis denotes the image position θ in the units of the Einstein radius. Top left: $n = 0.5$ Top right: $n = 1$. Bottom left: $n = 2$. Bottom right: $n = 3$. [44]

Table 3.1: The sign of the convergence κ. It is the same as that of $\varepsilon(1-n)$ according to Eq. (2.14). [44]

$\kappa > 0$	$\varepsilon > 0$ & $n < 1$ $\varepsilon < 0$ & $n > 1$
$\kappa = 0$	$n = 1$
$\kappa < 0$	$\varepsilon > 0$ & $n > 1$ $\varepsilon < 0$ & $n < 1$

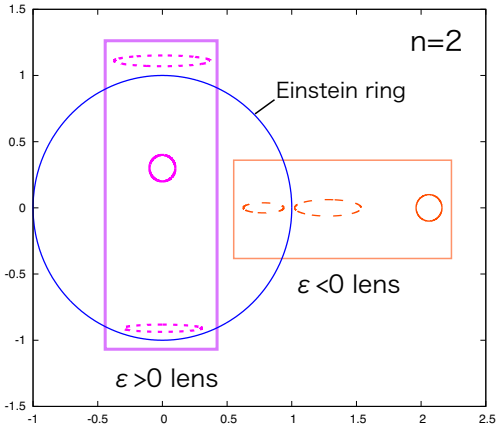

Figure 3.2: Numerical figures of lensed images for attractive ($\varepsilon > 0$) and repulsive ($\varepsilon < 0$) cases. They are denoted by dashed curves. We take $n = 2$. The source for each case is denoted by solid circles, which are located on the horizontal axis and vertical one for $\varepsilon < 0$ and $\varepsilon > 0$, respectively. [44]

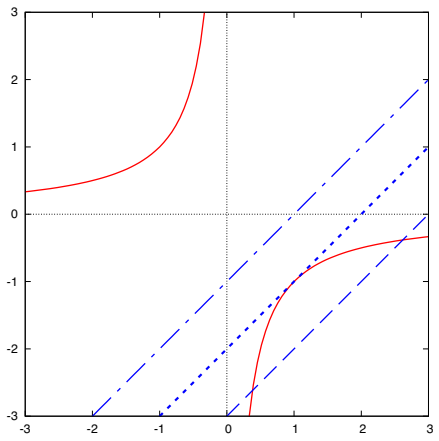

Figure 3.3: Repulsive lens model ($\varepsilon < 0$). Solid curves denote $1/\hat{\theta}^n$ and straight lines mean $\hat{\theta} - \hat{\beta}$. Their intersections correspond to image positions that are roots for the lens equation. There are three cases: No image for a small $\hat{\beta}$ (dot-dashed line), a single image for a particular $\hat{\beta}$ (dotted line), and two images for a large $\hat{\beta}$ (dashed line). The two images are on the same side of the lens object. [44]

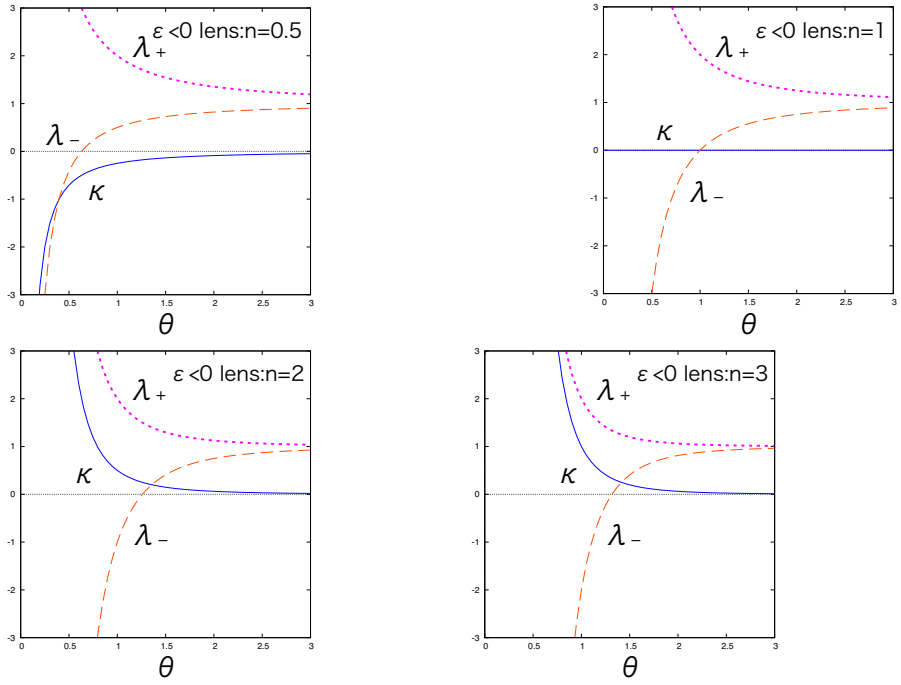

Figure 3.4: κ, λ_+ and λ_- for $\varepsilon < 0$. They are denoted by solid (blue in colors), dotted (purple in colors) and dashed (red in colors) curves, respectively. The horizontal axis denotes the image position θ in the units of the Einstein radius. Top left: $n = 0.5$ Top right: $n = 1$. Bottom left: $n = 2$. Bottom right: $n = 3$. [44]

Chapter 4

Microlensed image centroid motion by the modified spacetime

4.1 Modified spacetime model and modified lens equation

This section briefly summarizes the basics of the exotic lens models [36, 44].

4.1.1 Modified bending angle of light

Following Kitamura et al. [36], in the chapter2, we assumes that an asymptotically flat, static and spherically symmetric modified spacetime could depend on the inverse distance to the power of positive n in the weak field approximation. Note that some of the notations are different from those in Chapter 2. We consider the light propagation through a four-dimensional spacetime, though the whole spacetime may be higher dimensional. The four-dimensional spacetime metric is expressed as

$$ds^2 = -\left(1 - \frac{\varepsilon_1}{r^n}\right) dt^2 + \left(1 + \frac{\varepsilon_2}{r^n}\right) dr^2 + r^2(d\Theta^2 + \sin^2\Theta d\phi^2) + O(\varepsilon_1^2, \varepsilon_2^2, \varepsilon_1\varepsilon_2), \tag{4.1}$$

where r is the circumference radius and ε_1 and ε_2 are small book-keeping parameters in iterative calculations. The weak field approximation means $\varepsilon_1/r^n \ll 1$ and $\varepsilon_2/r^n \ll 1$. Namely, we study a far field from the lens object as $r \gg \varepsilon_1^{1/n}$ and $r \gg \varepsilon_2^{1/n}$. Note that Eq. (4.1) is not valid in the strong field near $r = 0$ (Please see [92] for more detail). Here, ε_1 and ε_2 may be either

positive or negative, respectively. Negative ε_1 and ε_2 for $n = 1$ correspond to a negative mass (in the linearized Schwarzschild metric).

Without loss of generality, we focus on the equatorial plane $\Theta = \pi/2$, since the spacetime is spherically symmetric. The deflection angle of light is obtained at the linear order as [36]

$$\alpha = \frac{\varepsilon}{b^n} \int_0^{\frac{\pi}{2}} \cos^n \psi d\psi + O(\varepsilon^2), \tag{4.2}$$

where the integral is positive definite, b denotes the impact parameter of the light ray, and we define $\varepsilon \equiv n\varepsilon_1 + \varepsilon_2$. By absorbing the positive integral into the parameter ε, we rewrite the linear-order deflection angle simply as $\alpha = \bar{\varepsilon}/b^n$, where the sign of $\bar{\varepsilon}$ is the same as that of ε. This deflection angle recovers the Schwarzschild ($n = 1$) and Ellis wormhole ($n = 2$) cases. For $\varepsilon > 0$, the deflection angle of light is always positive, which means that the corresponding spacetime model causes the gravitational pull on light rays. For $\varepsilon < 0$, on the other hand, it is inevitably negative, which implies the gravitational repulsion on light rays like a concave lens.

We mention an effective mass. A simple application of the standard lens theory [33] suggests that the deflection angle of light in the form of $\alpha = \bar{\varepsilon}/b^n$ corresponds to a convergence (scaled surface mass density) as

$$\kappa(b) = \frac{\bar{\varepsilon}(1-n)}{2} \frac{1}{b^{n+1}}, \tag{4.3}$$

which implies an extended spherical distribution of matter (or energy) for $n \neq 1$ and a singular source only for $n = 1$.

For the weak-field Schwarzschild case ($n = 1$), it follows that the convergence vanishes. For $\varepsilon > 0$ and $n > 1$, the effective surface mass density of the lens object is interpreted as negative in the framework of the standard lens theory [36]. This means that the matter (and energy) needs to be exotic if $\varepsilon > 0$ and $n > 1$. Also when $\varepsilon < 0$ and $n < 1$, the convergence is negative and hence the matter (and energy) needs to be exotic. Interestingly, when $\varepsilon < 0$ and $n > 1$, the convergence is positive everywhere except for the central singularity and hence exotic matter (and energy) is not required in the framework of the standard lens theory, in spite of the gravitational repulsion on light rays. Attraction ($\varepsilon > 0$) and repulsion ($\varepsilon < 0$) in the above two-parameter models do not have a one-to-one correspondence to positive convergence $\kappa > 0$ and negative one $\kappa < 0$. This point is summarized in Table 4.1 [44].

4.1.2 Modified Einstein radius

Under the thin lens approximation, it is useful to consider the lens equation as [33]

$$\beta = \frac{b}{D_L} - \frac{D_{LS}}{D_S}\alpha(b), \tag{4.4}$$

where β denotes the angular position of the source and D_L, D_S, D_{LS} are the distances from the observer to the lens, from the observer to the source, and from the lens to the source, respectively. Note that there is the mathematical consistency of the use of the lens equation Eq. (4.4), where the trigonometric functions are approximated by their leading terms. The present paper studies the leading term in the deflection angle, so that Eq. (4.4) can be mathematically consistent. On the other hand, if one wishes to include the next (and higher order) for the bending angle, the third-order (or higher-order) terms in the expansion of the trigonometric functions have to be taken into account in the lens equation, because of the mathematical consistency [9, 2, 3].

For $\varepsilon > 0$, there is always a positive root corresponding to the Einstein ring for $\beta = 0$. The Einstein ring radius is defined as [44]

$$\theta_E \equiv \left(\frac{\bar{\varepsilon} D_{LS}}{D_{\rm S} D_L^n}\right)^{\frac{1}{n+1}}. \tag{4.5}$$

If $\varepsilon < 0$, on the other hand, Eq. (4.4) has no positive root for $\beta = 0$. This is because this case describes the repulsive force. For later convenience in normalizing the lens equation, we define the (tentative) Einstein ring radius for $\varepsilon < 0$ as

$$\theta_E \equiv \left(\frac{|\bar{\varepsilon}| D_{LS}}{D_S D_L^n}\right)^{\frac{1}{n+1}}, \tag{4.6}$$

though the Einstein ring does not appear for this case. This radius gives a typical angular size for $\varepsilon < 0$ lenses.

Like Schwarzschild lenses, there might exist a photon sphere for $\varepsilon > 0$. The radius of the photon sphere for the spacetime metric by Eq. (4.1) might become

$$R_{ps} = \left(\frac{(n+2)\varepsilon_1}{2}\right)^{1/n}. \tag{4.7}$$

See [53] for a more thorough discussion on the photon surfaces.

4.1.3 Modified lens equation: $\varepsilon > 0$ case

Following Izumi et al. [44], let us begin with $\varepsilon > 0$ case. As already stated, the matter (and energy) needs to be exotic if $n > 1$. In the units of the

Einstein ring radius, Eq. (4.4) is rewritten in the vectorial form as

$$\hat{\boldsymbol{\beta}} = \hat{\boldsymbol{\theta}} - \frac{\hat{\boldsymbol{\theta}}}{\hat{\theta}^{n+1}} \quad (\hat{\theta} > 0), \tag{4.8}$$

$$\hat{\boldsymbol{\beta}} = \hat{\boldsymbol{\theta}} - \frac{\hat{\boldsymbol{\theta}}}{(-\hat{\theta})^{n+1}} \quad (\hat{\theta} < 0), \tag{4.9}$$

where we normalize $\hat{\beta} \equiv \beta/\theta_E$ and $\hat{\theta} \equiv \theta/\theta_E$ for the angular position of the image $\theta \equiv b/D_L$, and $\hat{\boldsymbol{\beta}}$ and $\hat{\boldsymbol{\theta}}$ denote the corresponding vectors. There is always one image for $\hat{\theta} > 0$, while the other image appears for $\hat{\theta} < 0$ [36].

4.1.4 Modified lens equation: $\varepsilon < 0$ case

Next, let us mention $\varepsilon < 0$ case [44]. In the units of the Einstein ring radius, Eq. (4.4) is rewritten in the vectorial form as

$$\hat{\boldsymbol{\beta}} = \hat{\boldsymbol{\theta}} + \frac{\hat{\boldsymbol{\theta}}}{\hat{\theta}^{n+1}} \quad (\hat{\theta} > 0), \tag{4.10}$$

$$\hat{\boldsymbol{\beta}} = \hat{\boldsymbol{\theta}} + \frac{\hat{\boldsymbol{\theta}}}{(-\hat{\theta})^{n+1}} \quad (\hat{\theta} < 0). \tag{4.11}$$

Without loss of generality, we assume $\hat{\beta} > 0$. Then, Eq. (4.11) has no root satisfying $\hat{\theta} < 0$, while Eq. (4.10) has at most two positive roots. Figure 4.1 shows that there are three cases of the image number. For a large impact parameter case, two images appear on the same side with respect to the lens position, while no image appears for a small impact parameter. The only one image appears only when the impact parameter takes a critical value. Let us focus on the two image cases, from which the single image case can be discussed in the limit as the impact parameter approaches the particular value.

4.2 Microlensed image centroid

4.2.1 Image centroid

Let us study the microlensed image centroid motions. In any case of $\varepsilon > 0$ and $\varepsilon < 0$, the image positions are denoted by $\hat{\boldsymbol{\theta}}_1$ and $\hat{\boldsymbol{\theta}}_2$, and the corresponding amplification factors are denoted by A_1 and A_2. Without loss of generality, we take $\hat{\theta}_1 > \hat{\theta}_2$. In analogy with the center of the mass distribution, the centroid position of the light distribution of a gravitationally

microlensed source is given by

$$\hat{\boldsymbol{\theta}}_{pc} = \frac{A_1\hat{\boldsymbol{\theta}}_1 + A_2\hat{\boldsymbol{\theta}}_2}{A_{tot}}, \tag{4.12}$$

where A_{tot} denotes the total amplification as $A_1 + A_2$. The corresponding scalar is defined as $\hat{\theta}_{pc} \equiv (A_1\hat{\theta}_1 + A_2\hat{\theta}_2)A_{tot}^{-1}$. Note that $\hat{\theta}_{pc}$ is positive, when the centroid is located on the same side of the source with respect to the lens center.

The relative displacement of the image centroid with respect to the source position is written as

$$\delta\hat{\boldsymbol{\theta}}_{pc} = \hat{\boldsymbol{\theta}}_{pc} - \hat{\boldsymbol{\beta}}. \tag{4.13}$$

Henceforth, this is referred to as the centroid shift. The corresponding scalar is defined as $\delta\hat{\theta}_{pc} \equiv \hat{\theta}_{pc} - \hat{\beta}$. $\delta\hat{\theta}_{pc}$ is positive, when $\hat{\theta}_{pc}$ is larger than $\hat{\beta}$.

By taking account of the relation between the lens and source trajectory in the sky, the time dependence of $\hat{\beta}$ is written as

$$\hat{\beta}(t) = \sqrt{\hat{\beta}_0^2 + (t - t_0)^2/{t_E}^2}, \tag{4.14}$$

where $\hat{\beta}_0$ is the impact parameter of the source trajectory and t_0 is the time of closest approach. Here, the source is assumed to be in uniform linear motion. We choose $t_0 = 0$. t_E is the Einstein radius crossing time given by

$$t_E = R_E/v_T, \tag{4.15}$$

where v_T is the transverse velocity of the lens relative to the source and observer. In the following numerical computations, time is normalized by the Einstein ring radius crossing time.

In making numerical figures, we employ $x - y$ coordinates, such that the coordinate origin is chosen as the lens center, x-axis is taken along the direction of the source motion and y-axis is perpendicular to the source motion.

4.2.2 Numerical computations: $\varepsilon > 0$ case

Let us begin with the $\varepsilon > 0$ case. See Figure 4.2 for the image centroid trajectories by $\varepsilon > 0$ models for $\hat{\beta}_0 = 0.3$ and 3. Figure 4.3 shows the image centroid shift by the $\varepsilon > 0$ models. For $\hat{\beta}_0 = 0.3$ for instance, the maximum vertical shift of the image centroid position by the exotic lens models is $0.2(n = 0.5)$, $0.14(n = 1)$, $0.07(n = 3)$ and $0.02(n = 10)$ in the units of the Einstein ring radius, respectively. For $\hat{\beta}_0 = 3$, it is nearly $0.5(n = 0.5)$, $0.3(n = 1)$, $-0.01(n = 3)$ and $-0.02(n = 10)$. These results suggest that

the astrometric lensing by the exotic models with large n is relatively weak compared with that by the Schwarzschild one ($n = 1$). In the weak-field region, one can understand the suppression of the anomalous shift of the image centroid position for large n, because the bending angle by the large n models is proportional to the inverse impact parameter to the power of n, whereas that by the Schwarzschild lens depends on the inverse impact parameter.

A distinctive feature is that in $\varepsilon > 0$ and $n > 2$ cases bow knots might be added into the centroid shift trajectory, while the trajectory is known to be an ellipse for $n = 1$ case [45, 49] and to be oval for $n = 2$ [19]. Such a multiply-connected shape of the centroid shift orbit would be an evidence of the corresponding exotic lens in astrometric observations. Figure 4.3 shows the bow-tie shape might disappear when the impact parameter becomes sufficiently large, for instance $\hat{\beta} \sim 3$. For $\varepsilon > 0$ and $n = 3$, the centroid shift could be negative for the $\hat{\beta}_0 = 3$ case. This is partly because A_2 becomes large compared with the $n = 1$ case.

At the center of the bow tie in the centroid shift, the image centroid position is the same as the intrinsic (unlensed) source position. At which time (and the corresponding source position) does the image centroid position agree with the source position? For Schwarzschild lens, the image centroid position agrees with the source position only at $t = \pm\infty$, namely $\beta = \infty$. In order to study this coincidence time (and source position), it is convenient to use Figure 4.4 for $\hat{\theta}_{pc}$ and $\hat{\beta}$ and Figure 4.5 for $\delta\hat{\theta}_{pc}$ and $\hat{\beta}$. Roughly speaking, the coincidence occurs at $\hat{\beta} \sim 1-3$, namely a few times the Einstein crossing time. This timescale might be used for applications to observations.

4.2.3 Numerical computations: $\varepsilon < 0$ case

Next, we consider the $\varepsilon < 0$ case. Figure 4.6 shows the image centroid motion by the $\varepsilon < 0$ models. Note that the centroid curve does not exist for small $\hat{\beta}$ because of no images. See also Figure 4.1 for no image cases. Such a peculiar event might be misinterpreted as an eclipse in astronomy.

Figure 4.7 shows the image centroid shift by the $\varepsilon < 0$ models. There does not appear any bow-tie shape. Note that the image centroid shift is always negative, because the effective force is repulsive. For unseen lens objects, the negative shift can be hardly distinguished from the positive one.

The centroid shift trajectory for the repulsive models might be elongated vertically to the source motion direction like a prolate spheroid as shown by Figure 4.7, whereas that for convex-type attractive models such as the Schwarzschild one is tangentially elongated like an oblate spheroid (See Figure 4.3). Figures 4.3 and 4.7 show that the size of the centroid shift by the

repulsive models for each n and $\hat{\beta}_0$ is comparable to that for the corresponding $\varepsilon > 0$ models.

4.2.4 Parameter estimations

Equations (4.5) and (4.6) are rewritten as

$$\begin{aligned} \frac{|\bar{\varepsilon}|}{R_E^n} &= \frac{D_S R_E}{D_{LS} D_L} \\ &= \frac{D_S \theta_E}{D_{LS}}. \end{aligned} \tag{4.16}$$

Here, D_L, D_S, D_{LS} and $R_E = D_L \theta_E$ are observables in astronomy, while $\bar{\varepsilon}$ and n are not direct observables but model parameters. Note that $\bar{\varepsilon}/R_E^n$ is comparable to the typical size of the deflection angle.

The right-hand side of Eq. (4.16) consists of the observables and it is a dimensionless quantity. Hence, Eq. (4.16) allows us to investigate $|\bar{\varepsilon}|/R_E^n$ from observations. See Tables 4.2 and 4.3 for Einstein ring size and Einstein radius crossing time, respectively. Near future astrometry space missions such as Gaia and JASMINE are expected to have angular sensitivity of a few micro arcseconds, for which the relevant parameter combination is limited as $|\bar{\varepsilon}|/R_E^n > 10^{-11}$. Roughly speaking, the mission life time is several years, for which the relevant timescale is limited as $t_E <$ a few years and Table 4.3 thus tells the limit as $|\bar{\varepsilon}|/R_E^n < 10^{-7}$ (for Bulge) and $< 10^{-8}$ (for LMC). In total, the parameter range relevant for the near future missions is $10^{-11} < |\bar{\varepsilon}|/R_E^n < 10^{-7}$.

Before closing this section, we mention how large n models could lead to a multiply-connected curve of the microlensed centroid shift. Numerical calculations suggest that $n > 2$ and $\varepsilon > 0$ models could produce a bow-tie shape. See also Figure 4.8 for numerical computations in the vicinity of $n = 2$ as $n = 2.0, 2.1, 2.2$ and 2.3. The numerical calculations suggest that the bow tie shape could appear, if $n > 2$. Numerical computations for other parameter values suggest that the maximum numbers of the loops and the knots in the the centroid curve are three and one, respectively, which are actually achieved by the $n = 3$ model.

4.3 Summary of this chapter

We examined gravitational lens models inspired by modified gravity theories, exotic matter and energy. By using an asymptotically flat, static and spherically symmetric spacetime model of which metric depends on the inverse

distance to the power of positive n, it was shown in the weak field and thin lens approximations that, for large n cases in the convex-type models, the centroid shift from the source position might move on a multiply-connected curve like a bow tie, while it is known to move on an ellipse for $n = 1$ case and to move on an oval curve for $n = 2$. This bow-tie shape by the convex-type exotic lens models is distinguishable from standard ones due to binary motions or due the microlensing by Schwarzschild lens. The distinctive feature such as the bow-tie shape may be used for searching (or constraining) localized exotic matter or energy with astrometric observations.

The parameter range relevant for the current and near-future missions such as Gaia and JASMIME is $10^{-11} < |\bar{\varepsilon}|/R_E^n < 10^{-7}$, where we assume that the accuracy in astrometry will reach a few micro arcseconds and the mission lifetime will be several years.

It was shown also that the centroid shift trajectory for concave-type repulsive models might be elongated vertically to the source motion direction like a prolate spheroid, whereas that for convex-type attractive models such as the Schwarzschild one is tangentially elongated like an oblate spheroid. The image centroid shift by the repulsive models is always negative, because the effective force is repulsive. For unseen lens objects, the negative shift can be hardly distinguished from the positive one. In this sense, it might be relatively difficult to investigate the repulsive models in astrometry.

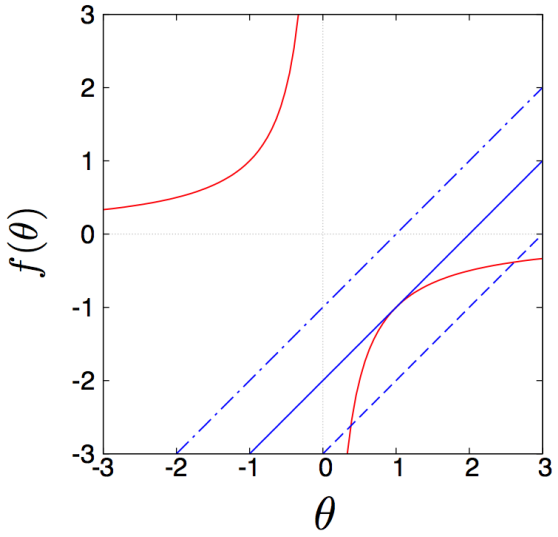

Figure 4.1: Repulsive lens model ($\varepsilon < 0$). Solid curves denote $1/\hat{\theta}^n$ and straight lines mean $\hat{\theta} - \hat{\beta}$. Their intersections correspond to image positions that are roots for the lens equation. There are three cases: No image for a small $\hat{\beta}$ (dot-dashed line), a single image for a particular $\hat{\beta}$ (dotted line), and two images for a large $\hat{\beta}$ (dashed line). The two images are on the same side of the lens object. [76]

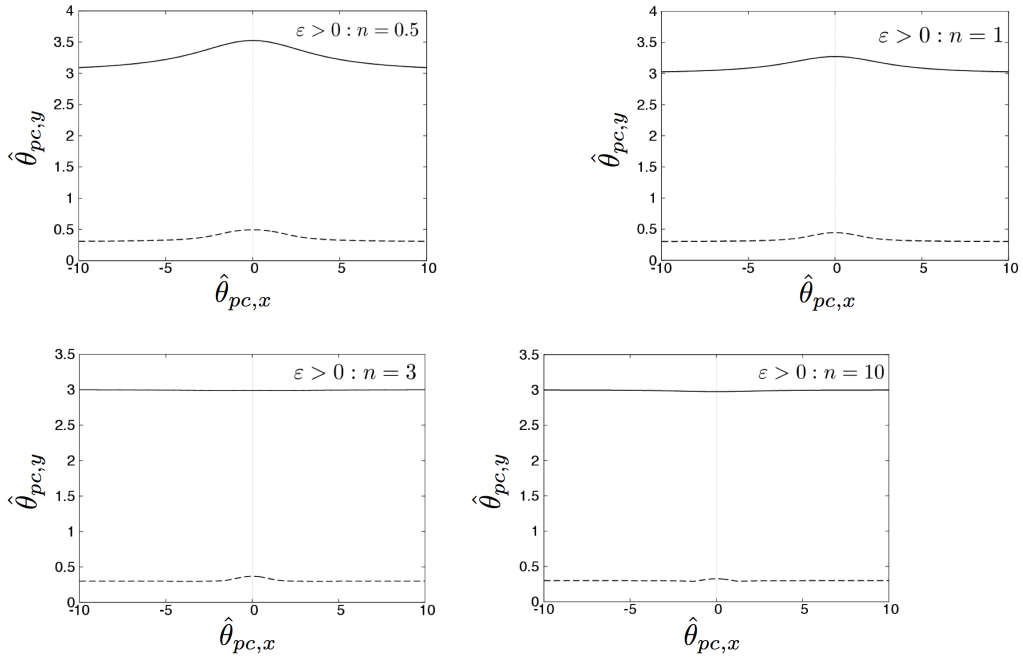

Figure 4.2: Centroid motions as $(\hat{\theta}_{pc,x}, \hat{\theta}_{pc,y})$ for $\varepsilon > 0$ (convex-type attractive models). The solid and dashed curves correspond to $\hat{\beta}_0 = 3$ and $\hat{\beta}_0 = 0.3$, respectively. The horizontal axis along the source linear motion is $\hat{\theta}_{pc,x}$ and the vertical axis is $\hat{\theta}_{pc,y}$. Top left: $n = 0.5$ Top right: $n = 1$. Bottom left: $n = 3$. Bottom right: $n = 10$. [76]

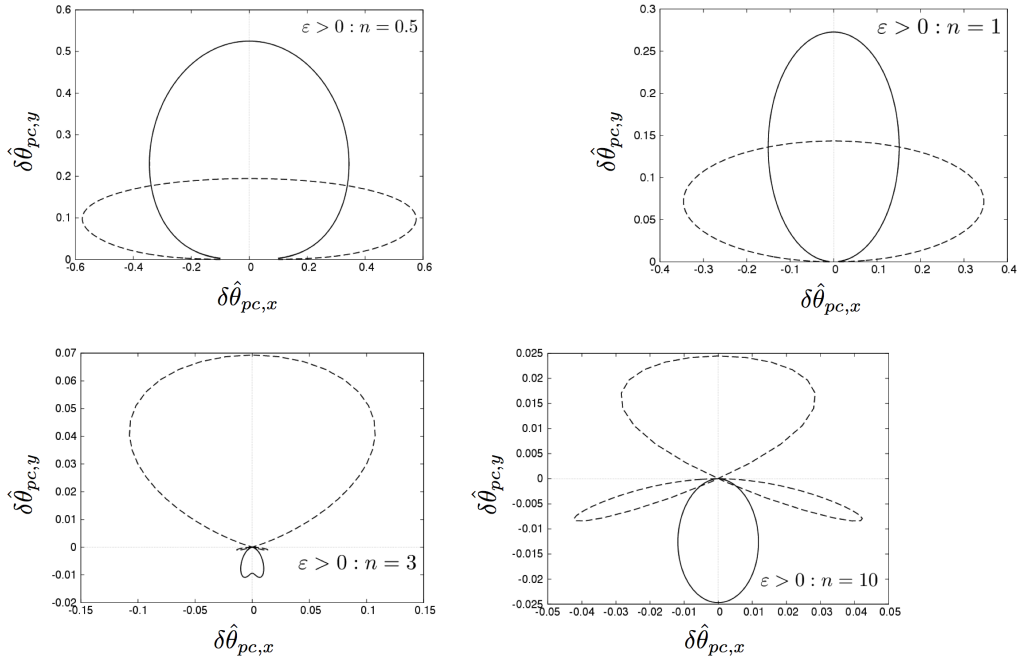

Figure 4.3: Centroid shifts $\delta\hat{\boldsymbol{\theta}}_{pc}$ for $\varepsilon > 0$ (convex-type attractive models). The solid and dashed curves correspond to $\hat{\beta}_0 = 3$ and $\hat{\beta}_0 = 0.3$, respectively. The horizontal axis along the source velocity is $\delta\hat{\theta}_{pc,x}$ and the vertical axis is $\delta\hat{\theta}_{pc,y}$. Top left: $n = 0.5$ Top right: $n = 1$. Bottom left: $n = 3$. Bottom right: $n = 10$. [76]

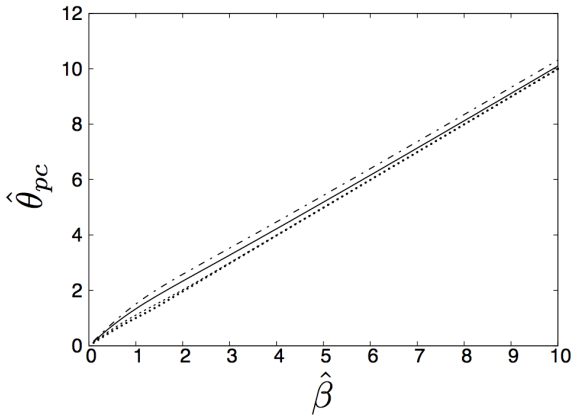

Figure 4.4: Image centroid $\hat{\theta}_{pc}$ and $\hat{\beta}$ for $\varepsilon > 0$ (convex-type attractive models). The dot-dashed, solid, dashed and dotted curves denote $n = 0.5$, 1, 3 and 10, respectively. The horizontal axis denotes the source position $\hat{\beta}$ normalized by the Einstein radius, and the vertical axis denotes $\hat{\theta}_{pc}$. [76]

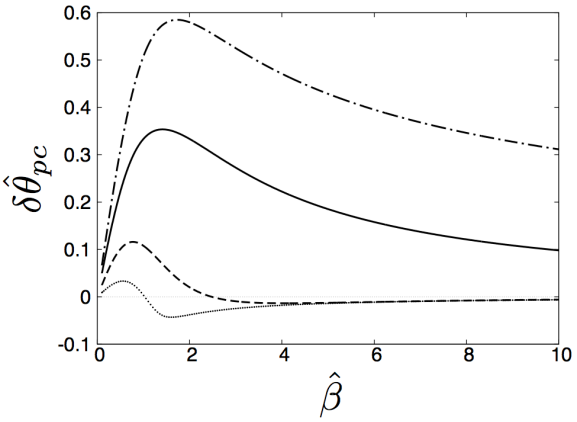

Figure 4.5: Image centroid shift $\delta\hat{\theta}_{pc}$ and $\hat{\beta}$ for $\varepsilon > 0$ (convex-type attractive models). The dot-dashed, solid, dashed and dotted curves denote $n = 0.5$, 1, 3 and 10, respectively. The horizontal axis denotes the source position $\hat{\beta}$ normalized by the Einstein radius, and the vertical axis denotes $\delta\hat{\theta}_{pc}$. [76]

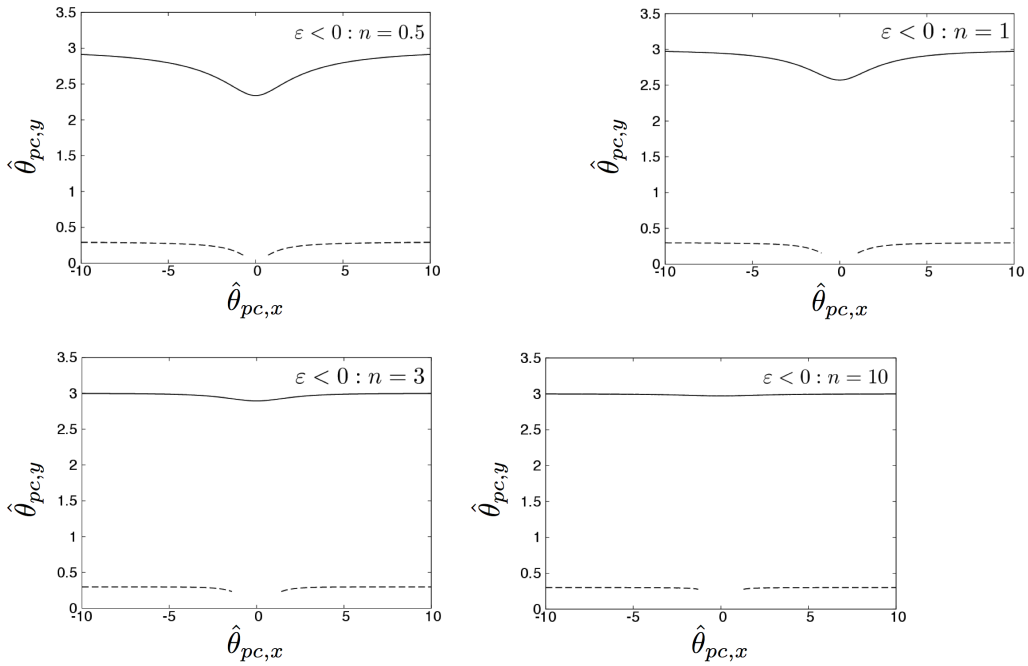

Figure 4.6: Centroid motions as $(\hat{\theta}_{pc,x}, \hat{\theta}_{pc,y})$ for $\varepsilon < 0$ (repulsive models). The solid and dashed curves correspond to $\hat{\beta}_0 = 3$ and $\hat{\beta}_0 = 0.3$, respectively. The horizontal axis along the source linear motion is $\hat{\theta}_{pc,x}$ and the vertical axis is $\hat{\theta}_{pc,y}$. The dashed curves do not exist for small $\hat{\beta}$, where no images appear. Top left: $n = 0.5$ Top right: $n = 1$. Bottom left: $n = 3$. Bottom right: $n = 10$. [76]

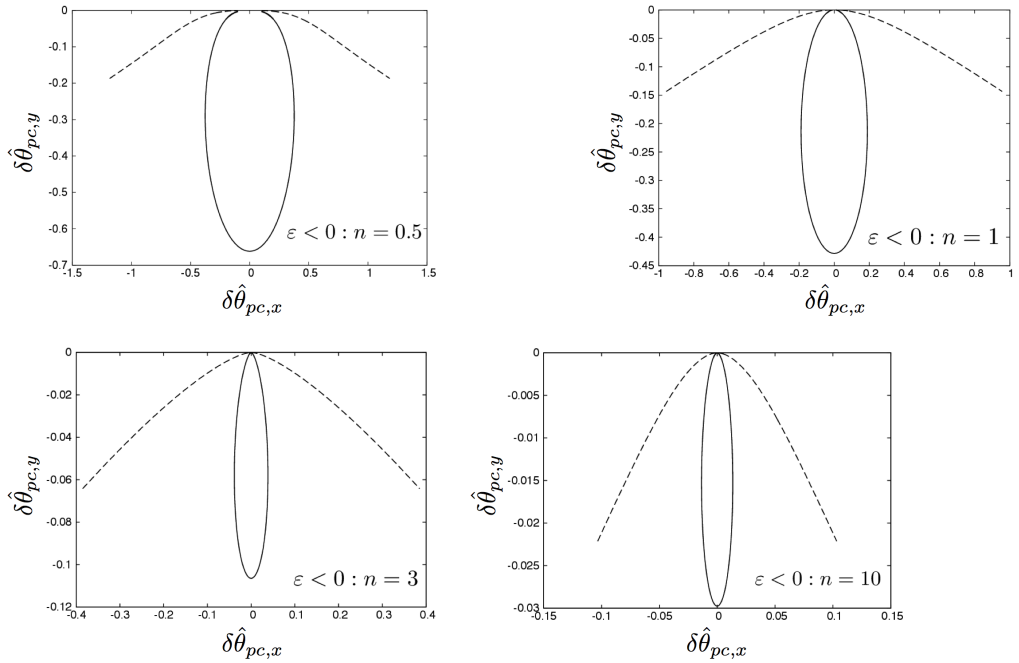

Figure 4.7: Centroid shifts $\delta\hat{\boldsymbol{\theta}}_{pc}$ for $\varepsilon < 0$ (concave-type repulsive models). The solid and dashed curves correspond to $\hat{\beta}_0 = 3$ and $\hat{\beta}_0 = 0.3$, respectively. The horizontal axis along the source velocity is $\delta\hat{\theta}_{pc,x}$ and the vertical axis is $\delta\hat{\theta}_{pc,y}$. The dashed curves are not closed, because no images appear for small $\hat{\beta}$. Top left: $n = 0.5$ Top right: $n = 1$. Bottom left: $n = 3$. Bottom right: $n = 10$. [76]

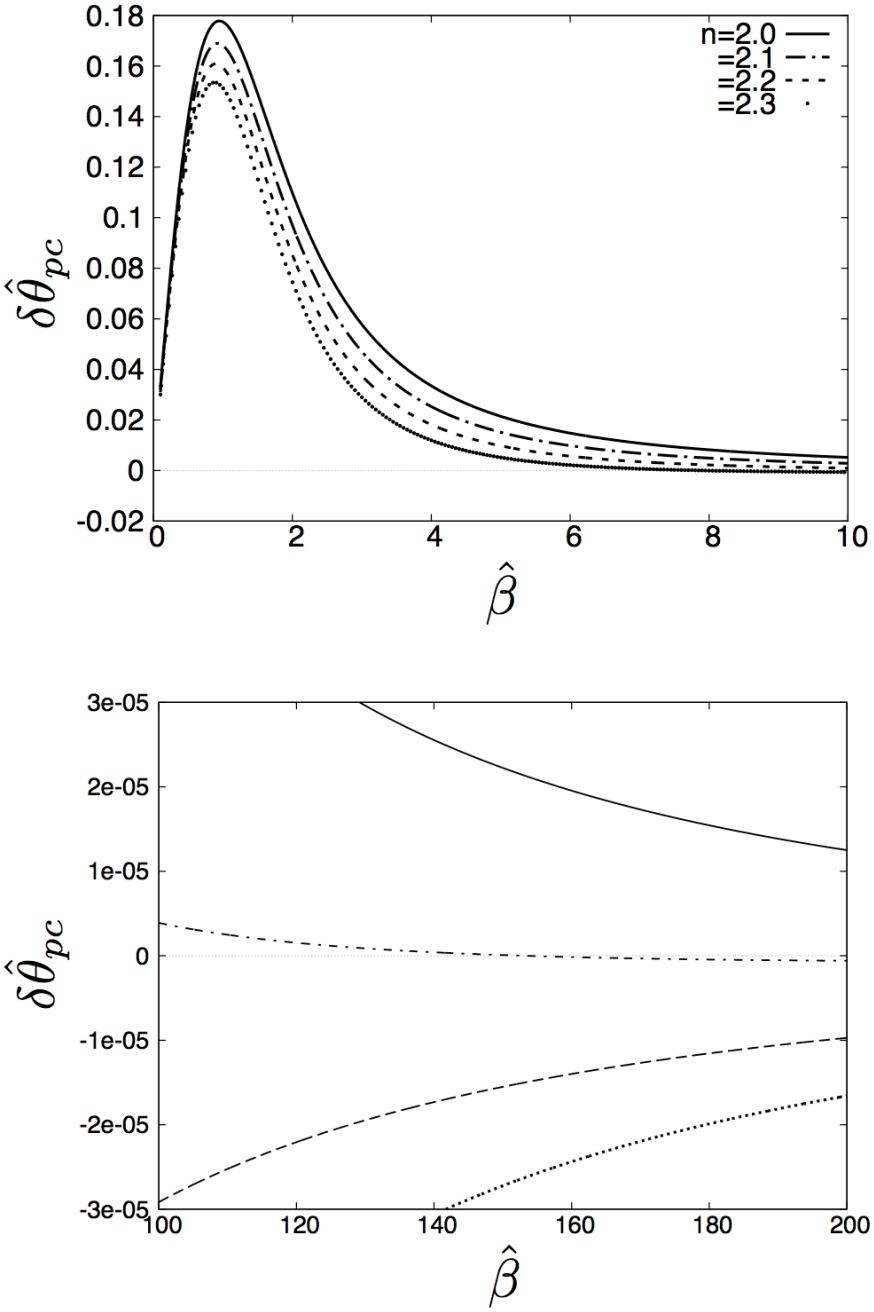

Figure 4.8: Image centroid shift $\delta\hat{\theta}_{pc}$ and $\hat{\beta}$ for $\varepsilon > 0$ (convex-type attractive models). The solid, dot-dashed, dashed and dotted curves denote $n = 2.0$, 2.1, 2.2 and 2.3, respectively. The horizontal axis denotes the source position $\hat{\beta}$ normalized by the Einstein radius, and the vertical axis denotes $\delta\hat{\theta}_{pc}$. Top: $\hat{\beta} \in [0, 10]$. Bottom: $\hat{\beta} \in [100, 200]$. [76]

Table 4.1: The sign of the convergence κ. It is the same as that of $\varepsilon(1-n)$ according to Eq. (2.14). [76]

$\kappa > 0$	$\varepsilon > 0$ & $n < 1$
	$\varepsilon < 0$ & $n > 1$
$\kappa = 0$	$n = 1$
$\kappa < 0$	$\varepsilon > 0$ & $n > 1$
	$\varepsilon < 0$ & $n < 1$

Table 4.2: Einstein radii and model parameters for Bulge and LMC lensings. θ_E is the angular Einstein radius, R_E is the Einstein radius, and $\bar{\varepsilon}$ and n are the two model parameters. $D_S = 8kpc$ and $D_L = 4kpc$ are assumed for Bulge. $D_S = 50kpc$ and $D_L = 25kpc$ are assumed for LMC. [76]

	Bulge		LMC	
$\theta_E(mas)$	$R_E(km)$	$\frac{\bar{\varepsilon}}{R_E^n}$	$R_E(km)$	$\frac{\bar{\varepsilon}}{R_E^n}$
10^{-3}	6.0×10^5	1.0×10^{-11}	3.7×10^6	1.0×10^{-11}
10^{-2}	6.0×10^6	1.0×10^{-10}	3.7×10^7	1.0×10^{-10}
10^{-1}	6.0×10^7	1.0×10^{-9}	3.7×10^8	1.0×10^{-9}
1	6.0×10^8	1.0×10^{-8}	3.7×10^9	1.0×10^{-8}
10	6.0×10^9	1.0×10^{-7}	3.7×10^{10}	1.0×10^{-7}
10^2	6.0×10^{10}	1.0×10^{-6}	3.7×10^{11}	1.0×10^{-6}
10^3	6.0×10^{11}	1.0×10^{-5}	3.7×10^{12}	1.0×10^{-5}

Table 4.3: Einstein radius crossing times for Bulge and LMC lensings. t_E is the Einstein radius crossing time. $D_S = 8kpc$ and $D_L = 4kpc$ are assumed for Bulge. $D_S = 50kpc$ and $D_L = 25kpc$ are assumed for LMC. $v_T = 220km/s$ is assumed for Bulge and LMC. In this table, the Einstein radius is calculated by $R_E = v_T \times t_E$ from the definition of the Einstein radius crossing time. Here, the input is $t_E \sim 10^{-3} - 10^3(day)$, namely $1(min.) - 3(yr.)$. [76]

$t_E(day)$	$R_E(km)$	$\frac{\bar{\varepsilon}}{R_E^n}$ [Bulge]	$\frac{\bar{\varepsilon}}{R_E^n}$ [LMC]
10^{-3}	1.9×10^4	3.1×10^{-13}	5.0×10^{-14}
10^{-2}	1.9×10^5	3.1×10^{-12}	5.0×10^{-13}
10^{-1}	1.9×10^6	3.1×10^{-11}	5.0×10^{-12}
1	1.9×10^7	3.1×10^{-10}	5.0×10^{-11}
10	1.9×10^8	3.1×10^{-9}	5.0×10^{-10}
10^2	1.9×10^9	3.1×10^{-8}	5.0×10^{-9}
10^3	1.9×10^{10}	3.1×10^{-7}	5.0×10^{-8}

Chapter 5

Gravitational lensing by Tangherlini spacetime

In this Chapter, we investigate the gravitational lensing effects in the weak field approximation and in the strong field limit of the Tangherlini spacetime [67]. The Tangherlini lens model would work as a wide-range toy model for the exotic lens objects with strong gravitational field since the Tangherlini spacetime is a solution of the Einstein equations in all dimensions. The Tangherlini lens model is expected to show the general features of the gravitational lensing effects by exotic gravitational objects in both the weak and strong gravitational field.

The gravitational lens in the strong field limit is related to the other phenomena such as the quasi-normal modes of a black hole [68, 69] and the high-energy absorption cross section [70] which are caused by the nature of the null geodesic near the photon sphere. Thus, the investigation of gravitational lensing effects of the all-dimensional black hole in the strong field limit would give us a new perspective on the intrinsic property of the all-dimensional black hole.

This Chapter is organized as follows. In Section 1, we review the null geodesic of the Tangherlini solution and investigate the deflection angle of light rays. In Section 2 and IV, we will investigate the deflection angle of the light in the weak field approximation and in the strong field limit, respectively. In Section 4, we study the gravitational lens effects in the strong field limit in the Tangherlini spacetime.

5.1 Deflection angle of light in Tangherlini spacetime

In this section, we review the null geodesic in the Tangherlini spacetime briefly and investigate the deflection angle of light rays. The Tangherlini solution is given by [67]

$$\begin{aligned} ds^2 &= -\left[1-\left(\frac{r_g}{r}\right)^{d-3}\right]dt^2 \\ &\quad + \frac{dr^2}{1-\left(\frac{r_g}{r}\right)^{d-3}} + r^2 d\sigma_{d-2}^2, \end{aligned} \tag{5.1}$$

where r_g is the event horizon radius and $d\sigma_{d-2}^2$ is

$$d\sigma_{d-2}^2 = d\theta_1^2 + \sum_{j=2}^{d-3}\prod_{i=1}^{j-1}\sin^2\theta_i d\theta_j^2 + \prod_{i=1}^{d-3}\sin^2\theta_i d\phi^2 \tag{5.2}$$

with the angular coordinates $\theta_i \in [0,\pi]$ and $\phi \in [0,2\pi]$ and the integer i runs from 1 into $d-3$. The event horizon exists at $r = r_g$, where r_g is given by

$$r_g = \frac{16\pi M}{(d-2)A_{d-2}}, \tag{5.3}$$

where M is the black hole mass and A_{d-2} is the area of the unit sphere which is given by

$$A_{d-2} = \frac{2\pi^{\frac{d-1}{2}}}{\Gamma\left(\frac{d-1}{2}\right)}. \tag{5.4}$$

For stationarity and axial symmetry, there exist the Killing vectors $t^\mu\partial_\mu = \partial_t$ and $\phi^\mu\partial_\mu = \partial_\phi$, respectively.

We set $\sin\theta_i = 1$ and consider the induced line element

$$ds^2 = -\left[1-\left(\frac{r_g}{r}\right)^n\right]dt^2 + \frac{dr^2}{1-\left(\frac{r_g}{r}\right)^n} + r^2 d\phi^2, \tag{5.5}$$

where $n \equiv d-3$. From $k^\mu k_\mu = 0$, where k^μ is the photon wave number, the equation of the photon trajectory is obtained by

$$\left(\frac{dr}{d\phi}\right)^2 = r^4 G(r,b), \tag{5.6}$$

where

$$G(r,b) \equiv \frac{1}{b^2} - \frac{1}{r^2} + \frac{r_g^n}{r^{n+2}} \tag{5.7}$$

and $b \equiv L/E$ is the impact parameter of the photon and $E \equiv -g_{\mu\nu}t^\mu k^\nu$, and $L \equiv g_{\mu\nu}\phi^\mu k^\nu$ are the energy and the angular momentum of the photon, respectively. We assume that the conserved energy E is positive. We can assume $L > 0$ or $b > 0$ without loss of generality.

The equation $G(r,b) = 0$ has two positive solutions $r = r_-$ and r_0 for $b > b_c$, one positive solution $r = r_- = r_0$ for $b = b_c$ and no positive solution for $b < b_c$, where

$$b_c \equiv \left(\frac{n+2}{n}\right)^{\frac{1}{2}} \left(\frac{n+2}{2}\right)^{\frac{1}{n}} r_g \tag{5.8}$$

is the critical impact parameter. From Eqs. (5.6) and (5.7), we find that the photon is scattered if $b > b_c$ while it reaches the event horizon $r = r_g$ if $b < b_c$.

We will assume $b_c < b$ in what follows since we are interested in the scattering problem. Here we define r_0 as the larger solution of the equation $G(r,b) = 0$ i.e. $0 < r_- \leq r_0$. Thus, r_0 is the closest distance of a photon. From $G(r_0,b) = 0$, the relation between the impact parameter b and the closest distance r_0 is given by

$$\frac{1}{b^2} = \frac{1}{r_0^2}\left[1 - \left(\frac{r_g}{r_0}\right)^n\right]. \tag{5.9}$$

The derivative of $G(r,b)$ with respect to r is given by

$$\frac{\partial G(r,b)}{\partial r} = \frac{2}{r^3} - (n+2)\frac{r_g^n}{r^{n+3}}. \tag{5.10}$$

Thus, the radius of the photon sphere which satisfies $\partial G(r_m,b)/\partial r = 0$ is obtained by

$$r_m = \left(\frac{n+2}{2}\right)^{\frac{1}{n}} r_g. \tag{5.11}$$

The deflection angle α is given by

$$\alpha = I(b) - \pi, \tag{5.12}$$

where

$$I(b) \equiv 2\int_{r_0}^{\infty} \frac{dr}{r^2\sqrt{G(r,b)}}. \tag{5.13}$$

5.2 Deflection angle in weak field approximation

In this section, we will calculate the deflection angle in the Tangherlini spacetime in weak field approximation by Keeton and Petters's method [71]. We define a small amount h by

$$h \equiv \left(\frac{r_g}{r_0}\right)^n \ll \left(\frac{r_g}{r_m}\right)^n = \frac{2}{n+2}. \tag{5.14}$$

The relation between the impact parameter b and the closet distance r_0 (5.9) is expressed by

$$\left(\frac{r_0}{b}\right)^2 = 1 - h. \tag{5.15}$$

Thus,

$$h = \left(\frac{r_g}{b}\right)^n + O(h^2). \tag{5.16}$$

Using $x \equiv r_0/r$, the deflection angle α is given by

$$\alpha = 2\int_0^1 \frac{dx}{\sqrt{1-x^2}\sqrt{1-hf(x)}} - \pi, \tag{5.17}$$

where

$$f(x) \equiv \frac{1-x^{n+2}}{1-x^2} = \frac{1+x+x^2+\cdots+x^{n+1}}{1+x}. \tag{5.18}$$

$f(x)$ monotonically increases in the range of $0 \leq x \leq 1$ with the minimum value $f(0) = 1$ and the maximum value $f(1) = (n+2)/2$.

We will consider the Taylor series by the term of 1st degree

$$(1-hf(x))^{-\frac{1}{2}} = 1 + \frac{1}{2}hf(x) + O(h^2) \tag{5.19}$$

with respect to

$$hf(x) \ll \left(\frac{r_g}{r_m}\right)^n f(1) = 1. \tag{5.20}$$

Therefore, the deflection angle of the light is given by

$$\alpha = 2\int_0^1 \frac{dx}{\sqrt{1-x^2}} + h\int_0^1 \frac{1-x^{n+2}}{(1-x^2)^{\frac{3}{2}}}dx - \pi + O(h^2). \tag{5.21}$$

We can easily integrate the first term,

$$\int_0^1 \frac{dx}{\sqrt{1-x^2}} = [\arcsin x]_0^1 = \frac{\pi}{2}. \tag{5.22}$$

Thus, the deflection angle is given by

$$\begin{aligned} \alpha &= H_{n+2}h + O(h^2) \\ &= H_{n+2}\left(\frac{r_g}{b}\right)^n + O\left(\left(\frac{r_g}{b}\right)^{2n}\right), \end{aligned} \tag{5.23}$$

where

$$H_m \equiv \int_0^{\frac{\pi}{2}} \frac{1-\sin^m k}{\cos^2 k} dk, \tag{5.24}$$

where $k \equiv \arcsin x$ and m is a positive integer.

A recurrence formula is obtained by

$$H_{n+2} = H_n + B_n, \tag{5.25}$$

where B_n is

$$\begin{aligned} B_n &\equiv \int_0^{\frac{\pi}{2}} \sin^n k dk = \int_0^{\frac{\pi}{2}} \cos^n k dk \\ &= \frac{\sqrt{\pi}}{2}\frac{\Gamma\left(\frac{n+1}{2}\right)}{\Gamma\left(\frac{n+2}{2}\right)} \\ &= \begin{cases} \frac{(n-1)!!}{n!!}\frac{\pi}{2} & \text{for an even } n, \\ \frac{(n-1)!!}{n!!} & \text{for an odd } n. \end{cases} \end{aligned} \tag{5.26}$$

When n is even, we can put $n = 2L$ where L is a positive integer. From $H_2 = \pi/2$ and Eqs. (5.25) and (5.26), we obtain

$$H_{n+2} = H_2 + \sum_{m=1}^{L} B_{2m} = \frac{\pi}{2}\left[1 + \sum_{m=1}^{L} \frac{(2m-1)!!}{(2m)!!}\right]. \tag{5.27}$$

Thus, the deflection angle is obtained by

$$\alpha = \frac{\pi}{2}\left[1 + \sum_{m=1}^{L} \frac{(2m-1)!!}{(2m)!!}\right]\left(\frac{r_g}{b}\right)^n + O\left(\left(\frac{r_g}{b}\right)^{2n}\right). \tag{5.28}$$

When n is odd, we can put $n = 2L-1$. From $H_1 = 1$ and Eqs. (5.25) and (5.26), we get

$$H_{n+2} = H_1 + \sum_{m=1}^{L} B_{2m-1} = 1 + \sum_{m=1}^{L} \frac{(2m-2)!!}{(2m-1)!!}. \tag{5.29}$$

Here we have defined $0!! = 1$. Thus, the deflection angle is

$$\alpha = \left[1 + \sum_{m=1}^{L} \frac{(2m-2)!!}{(2m-1)!!}\right] \left(\frac{r_g}{b}\right)^n + O\left(\left(\frac{r_g}{b}\right)^{2n}\right). \tag{5.30}$$

We can also calculate the deflection angle by the terms of higher order than the 1st degree with respect to h by Keeton and Petters's method [71].

5.3 Deflection angle in strong field limit

In this section, we will investigate the deflection angle in the Tangherlini spacetime in the strong field limit. We will express the deflection angle α of the light ray in the strong field limit by

$$\alpha(b) = -\bar{a} \log\left(\frac{b}{b_c} - 1\right) + \bar{b} + O\left((b - b_c)^{\frac{1}{2}}\right), \tag{5.31}$$

or

$$\alpha(\theta) = -\bar{a} \log\left(\frac{\theta D_l}{b_c} - 1\right) + \bar{b} + O\left((\theta D_l - b_c)^{\frac{1}{2}}\right), \tag{5.32}$$

where $\bar{a}$ is a positive parameter, $\bar{b}$ is a parameter, θ is the image angle and D_l is the distance between the observer and the lens object. For the small image angle $\theta \ll 1$, the impact parameter b can be described by

$$b = \theta D_l. \tag{5.33}$$

If we get the explicit expression for the deflection angle in the strong field limit, we can calculate countably infinite relativistic images angle θ_N and the countably infinite magnifications μ_N individually [63].

We show the explicit expression for the divergent part of the deflection angle in the all-dimensional Tangherlini spacetime or the parameter $\bar{a}$ and we integrate the regular part of the deflection angle in 4, 5 and 7 dimension.[1]

Using by Eqs. (5.9) and

$$z \equiv 1 - \left(\frac{r_0}{r}\right)^n, \tag{5.34}$$

[1]As below, we obey the convention of the analysis in the strong field limit but the definitions of some symbols such as z are different from the definitions by Bozza [63].

we rewrite $G(r,b)$ and $I(b)$ into $G(z,r_0)$ and $I(r_0)$, respectively, as follow:

$$\begin{aligned} G(z,r_0) &= \frac{1}{r_0^2}\left\{1-\left(\frac{r_g}{r_0}\right)^n \right. \\ &\quad \left. +(1-z)^{\frac{2}{n}}\left[-1+\left(\frac{r_g}{r_0}\right)^n(1-z)\right]\right\}. \end{aligned} \tag{5.35}$$

$$I(r_0) = \int_0^1 R(z) f(z,r_0) dz, \tag{5.36}$$

where

$$R(z) \equiv \frac{2}{n}(1-z)^{\frac{1}{n}-1} \tag{5.37}$$

and

$$\begin{aligned} f(z,r_0) &\equiv \frac{1}{\sqrt{r_0^2 G(z,r_0)}} \\ &= \frac{1}{\sqrt{1-\left(\frac{r_g}{r_0}\right)^n + (1-z)^{\frac{2}{n}}\left[-1+\left(\frac{r_g}{r_0}\right)^n(1-z)\right]}}. \end{aligned} \tag{5.38}$$

We can expand $r_0^2 G(z,r_0)$ near the $z=0$ and obtain

$$r_0^2 G(z,r_0) = \gamma(r_0) z + \beta(r_0) z^2 + \cdots, \tag{5.39}$$

where

$$\gamma(r_0) \equiv \frac{1}{n}\left[2-(n+2)\left(\frac{r_g}{r_0}\right)^n\right] \tag{5.40}$$

$$\beta(r_0) \equiv \frac{1}{n^2}\left[n-2+(n+2)\left(\frac{r_g}{r_0}\right)^n\right]. \tag{5.41}$$

Near the photon sphere $r_0 = r_m$, $\gamma(r_0)$ and $\beta(r_0)$ are expanded in a series,

$$\gamma(r_0) = \frac{2}{r_m}(r_0 - r_m) + O\left((r_0-r_m)^2\right) \tag{5.42}$$

and

$$\beta(r_0) = \frac{1}{n} - \frac{2}{n r_m}(r_0 - r_m) + O\left((r_0-r_m)^2\right), \tag{5.43}$$

respectively.

We will divide $I(r_0)$ into the divergent part $I_D(r_0)$ and the regular part $I_R(r_0)$ or

$$I(r_0) = I_D(r_0) + I_R(r_0). \tag{5.44}$$

The divergent part $I_D(r_0)$ is defined by

$$I_D(r_0) \equiv \int_0^1 R(0) f_0(z, r_0) dz, \tag{5.45}$$

where

$$f_0(z, r_0) \equiv \frac{1}{\sqrt{\gamma(r_0)z + \beta(r_0)z^2}}. \tag{5.46}$$

The divergent part $I_D(r_0)$ is calculated in a simple and straightforward way,

$$\begin{aligned} & I_D(r_0) \\ &= \frac{2}{n\sqrt{\beta(r_0)}} \log \left| \frac{\gamma(r_0) + 2\beta(r_0) + 2\sqrt{(\gamma(r_0) + \beta(r_0))\beta(r_0)}}{\gamma(r_0)} \right| \\ &= \frac{4}{n\sqrt{\beta(r_0)}} \log \left(\frac{\sqrt{\beta(r_0)} + \sqrt{\gamma(r_0) + \beta(r_0)}}{\sqrt{\gamma(r_0)}} \right). \end{aligned} \tag{5.47}$$

Therefore, the divergent part $I_D(r_0)$ in the strong field limit is obtained by

$$I_D(r_0) = -\frac{2}{\sqrt{n}} \log \left(\frac{r_0}{r_m} - 1 \right) + \frac{2}{\sqrt{n}} \log \frac{2}{n} + O(r_0 - r_m). \tag{5.48}$$

We will rewrite the divergent part $I_D(r_0)$ into a function $I_D(b)$ with respect to the impact parameter b since the lens equation is usually written as an equation in terms of the impact parameter b or the image angle θ. From the relation between the impact parameter b and the closet distance r_0 (5.9), we can regard the impact parameter $b(r_0)$ as a function with respect to the closet distance r_0, we expand the impact parameter $b(r_0)$ in a series near $r_0 = r_m$ and we get

$$\begin{aligned} b(r_0) &= b_c + \frac{1}{2} \left(\frac{n+2}{n} \right)^{\frac{3}{2}} \frac{n}{r_m} (r_0 - r_m)^2 \\ &\quad + O\left((r_0 - r_m)^3 \right). \end{aligned} \tag{5.49}$$

From Eqs. (5.8), (5.11) and (5.49) we obtain

$$\begin{aligned}\log\left(\frac{r_0}{r_m}-1\right) &= \frac{1}{2}\log\left(\frac{b}{b_c}-1\right)+\frac{1}{2}\log\left(\frac{2}{n+2}\right)\\ &\quad +O(r_0-r_m).\end{aligned} \tag{5.50}$$

Hence, the divergent part is

$$\begin{aligned}I_D(b) &= -\frac{1}{\sqrt{n}}\log\left(\frac{b}{b_c}-1\right)+\frac{1}{\sqrt{n}}\log\frac{2(n+2)}{n^2}\\ &\quad +O\left((b-b_c)^{\frac{1}{2}}\right).\end{aligned} \tag{5.51}$$

The regular part $I_R(r_0)$ is defined by

$$I_R(r_0)\equiv\int_0^1 g(z,r_0)dz, \tag{5.52}$$

where

$$g(z,r_0)\equiv R(z)f(z,r_0)-R(0)f_0(z,r_0). \tag{5.53}$$

We can expand $I_R(r_0)$ in powers of (r_0-r_m) and express it as a function $I_R(b)$ with respect to b as follow:

$$\begin{aligned}I_R(r_0) &= \sum_{l=0}^{\infty}\frac{1}{l!}(r_0-r_m)^l\int_0^1\left.\frac{\partial^l g}{\partial r_0^l}\right|_{r_0=r_m}dz\\ &= \frac{2}{n}\int_0^1\left[\frac{\sqrt{n+2}(1-z)^{\frac{1}{n}-1}}{\sqrt{n-(1-z)^{\frac{2}{n}}(n+2z)}}-\frac{\sqrt{n}}{z}\right]dz\\ &\quad +O(r_0-r_m)\\ &= 2\sqrt{n+2}\int_0^1\frac{dy}{\sqrt{n-(n+2)y^2+2y^{n+2}}}\\ &\quad -\frac{2\sqrt{n}}{n}\int_0^1\frac{dz}{z}+O\left((b-b_c)^{\frac{1}{2}}\right)\\ &= I_R(b),\end{aligned} \tag{5.54}$$

where we have used $y\equiv(1-z)^{\frac{1}{n}}$.

Thus, the deflection angle $\alpha(b)$ of the light on the Tangherlini spacetime in the strong field limit is obtained by

$$\begin{aligned}\alpha(b) &= I_D(b)+I_R(b)-\pi\\ &= -\frac{1}{\sqrt{n}}\log\left(\frac{b}{b_c}-1\right)+\frac{1}{\sqrt{n}}\log\frac{2(n+2)}{n^2}\\ &\quad +I_R(b)-\pi+O\left((b-b_c)^{\frac{1}{2}}\right).\end{aligned} \tag{5.55}$$

Hence, we get the parameters $\bar{a} = \frac{1}{\sqrt{n}}$ and $\bar{b} = \frac{1}{\sqrt{n}} \log \frac{2(n+2)}{n^2} + I_R(b) - \pi$.

We can analytically calculate the regular parts $I_R(b)$ for $n = 1$, 2 and 4 since the elliptic functions $I(b)$ for $n = 1$, 2 and 4 are integrable [27].

5.3.1 $n = 1$

We consider the case for $n = 1$. In this case, the critical impact parameter and the radius of the photon sphere are given by $b_c = \frac{3\sqrt{3}r_g}{2}$ and $r_m = \frac{3r_g}{2}$, respectively. The divergent part is obtained by

$$I_D(b) = -\log\left(\frac{b}{b_c} - 1\right) + \log 6 + O\left((b - b_c)^{\frac{1}{2}}\right). \tag{5.56}$$

The regular part $I_R(b)$ is given by

$$\begin{aligned} I_R(b) &= 2\int_0^1 \left(\frac{1}{z\sqrt{1 - \frac{2}{3}z}} - \frac{1}{z}\right) dz + O\left((b - b_c)^{\frac{1}{2}}\right) \\ &= 2\log\left[6\left(2 - \sqrt{3}\right)\right] + O\left((b - b_c)^{\frac{1}{2}}\right). \end{aligned} \tag{5.57}$$

Thus, the deflection angle $\alpha(b)$ of the light is obtained by

$$\begin{aligned} \alpha(b) &= I_D(b) + I_R(b) - \pi \\ &= -\log\left(\frac{b}{b_c} - 1\right) + \log\left[216\left(7 - 4\sqrt{3}\right)\right] \\ &\quad -\pi + O\left((b - b_c)^{\frac{1}{2}}\right). \end{aligned} \tag{5.58}$$

Therefore, we get the parameters $\bar{a} = 1$ and $\bar{b} = \log\left[216\left(7 - 4\sqrt{3}\right)\right] - \pi \simeq -0.40$. It recovers the deflection angle of the light in Schwarzschild spacetime in the strong field limit which was obtained by Bozza [63].

5.3.2 $n = 2$

For $n = 2$. the critical impact parameter and the radius of the photon sphere are $b_c = 2r_g$ and $r_m = \sqrt{2}r_g$, respectively. The divergent part is given by

$$\begin{aligned} I_D(b) &= -\frac{1}{\sqrt{2}} \log\left(\frac{b}{b_c} - 1\right) + \frac{1}{\sqrt{2}} \log 2 \\ &\quad + O\left((b - b_c)^{\frac{1}{2}}\right). \end{aligned} \tag{5.59}$$

The regular part is obtained by

$$\begin{aligned} I_R(b) &= \int_0^1 \left(\frac{\sqrt{2}}{z\sqrt{1-z}} - \frac{\sqrt{2}}{z} \right) dz + O\left((b-b_c)^{\frac{1}{2}} \right) \\ &= 2\sqrt{2}\log 2 + O\left((b-b_c)^{\frac{1}{2}} \right). \end{aligned} \tag{5.60}$$

Thus, we obtain the deflection angle $\alpha(b)$ in the strong field limit for $n = 2$;

$$\begin{aligned} \alpha(b) &= -\frac{1}{\sqrt{2}} \log\left(\frac{b}{b_c} - 1 \right) + \frac{5\sqrt{2}}{2}\log 2 - \pi \\ &\quad + O\left((b-b_c)^{\frac{1}{2}} \right). \end{aligned} \tag{5.61}$$

In this case, the parameters are given by $\bar{a} = \frac{1}{\sqrt{2}}$ and $\bar{b} = \frac{5\sqrt{2}}{2}\log 2 - \pi \sim -0.69$.

5.3.3 $n = 4$

For $n = 4$, the critical impact parameter and the radius of the photon sphere are given by $b_c = \left(\frac{27}{4}\right)^{\frac{1}{4}} r_g$ and $r_m = 3^{\frac{1}{4}} r_g$, respectively. The divergent part is obtained by

$$\begin{aligned} I_D(b) &= -\frac{1}{2}\log\left(\frac{b}{b_c} - 1 \right) + \frac{1}{2}\log\frac{3}{4} \\ &\quad + O\left((b-b_c)^{\frac{1}{2}} \right). \end{aligned} \tag{5.62}$$

The regular part $I_R(b)$ is given by

$$\begin{aligned} I_R(b) &= 2\sqrt{3}\int_0^1 \frac{dy}{\sqrt{2-3y^2+y^6}} - \int_0^1 \frac{dz}{z} + O\left((b-b_c)^{\frac{1}{2}} \right) \\ &= \log 12 + O\left((b-b_c)^{\frac{1}{2}} \right) \end{aligned} \tag{5.63}$$

and the deflection angle in the strong field limit is obtained by

$$\alpha(b) = -\frac{1}{2}\log\left(\frac{b}{b_c} - 1 \right) + \log 6\sqrt{3} - \pi + O\left((b-b_c)^{\frac{1}{2}} \right) \tag{5.64}$$

and hence we get the parameter $\bar{a} = \frac{1}{2}$ and $\bar{b} = +\log 6\sqrt{3} - \pi \sim -0.80$.

5.4 Gravitational Lensing

5.4.1 Lens equation

We consider the lens configuration which is given in Figure 5.1 The light ray emitted by the source S bends near the lensing object L. The observer O does not see the source S with the source angle ϕ but the image I with the image angle θ. For simplicity, we assume that both the observer O and the source S are far from the lensing object L or $D_l \gg b$ and $D_{ls} \gg b$, where D_l and D_{ls} are the distance between the observer O and the lensing object L and between the lensing object L and the source object S. We also assume the thin lens approximation that the light ray bends on the lens plane. The impact parameter b of the light ray is described by $b = D_l\theta$. Under the assumptions, the effective deflection angle $\bar{\alpha}$, the source angle ϕ and the image angle θ are small or $|\bar{\alpha}| \ll 1$, $|\phi| \ll 1$ and $|\theta| \ll 1$. The effective deflection angle $\bar{\alpha}$ is defined by

$$\bar{\alpha} \equiv (\alpha \bmod 2\pi). \tag{5.65}$$

The deflection angle α is expressed by

$$\alpha = \bar{\alpha} + 2\pi N, \tag{5.66}$$

where N is a non-negative integer which denotes the winding number of the light ray.

Then, the lens equation is given by

$$D_{ls}\bar{\alpha} = D_s(\theta - \phi), \tag{5.67}$$

where D_s is the separation between the observer O and the source S and satisfies the relation $D_s = D_l + D_{ls}$. If the source angle $\phi = 0$, ring-shaped images which are called the Einstein ring with the angle θ_0 for $N = 0$ and the relativistic Einstein ring with the angle $\theta_{N\geq 1}$ for $N \geq 1$ appear from the symmetry. From $N = 0$, $\phi = 0$ and Eqs. (5.23), (5.33), (5.66) and (5.67), the Einstein ring angle is given by

$$\theta_0 \sim \left(H_{n+2}\frac{D_{ls}}{D_s}\right)^{\frac{1}{n+1}} \left(\frac{r_g}{D_l}\right)^{\frac{n}{n+1}}. \tag{5.68}$$

The behaviors of the Tangherlini lens model in the weak field approximation has known already because the lens model is included in the exotic lens model or the general spherical lens model [36, 21, 44, 76]. Here, we refer only to the image angles and the magnification in the directly aligned

limit ($|\phi| \ll \theta_0 \ll 1$). Under the weak approximation, the lens equation has two solutions θ_{0+} and θ_{0-} regardless of the source angle ϕ for $n \geq 1$. For $|\phi| \ll \theta_0 \ll 1$, the image angles $\theta_{0\pm}$ and the magnification $\mu_{0\pm}$ are given by [36, 21]

$$\theta_{0\pm} = \pm\theta_0 + \frac{\phi}{1+n} \pm \frac{n\phi^2}{2(1+n)^2\theta_0} + O\left(\frac{\phi^3}{\theta_0^2}\right) \tag{5.69}$$

and

$$\mu_{0\pm} \sim \frac{1}{1+n}\frac{\phi \pm \theta_0}{\phi}, \tag{5.70}$$

respectively. The total magnification μ_0 in the directly aligned limit is given by

$$\mu_0 \equiv |\mu_{0+}| + |\mu_{0-}| = \frac{2}{1+n}\frac{\theta_0}{\phi}. \tag{5.71}$$

The relativistic Einstein rings or the relativistic images always appear on the region just outside the photon sphere. The angle of the innermost relativistic Einstein ring is obtained by

$$\theta_\infty = \frac{b_c}{D_l} = \left(1+\frac{2}{n}\right)^{\frac{1}{2}}\left(1+\frac{n}{2}\right)^{\frac{1}{n}}\frac{r_g}{D_l}. \tag{5.72}$$

The relation between the Einstein ring angle θ_0, the relativistic Einstein ring angle θ_∞ and the relativistic image angle $\theta_{N\geq 1}(\phi)$ is obtained by

$$\begin{aligned}\theta_{N\geq 1}(\phi) &\sim \theta_\infty \\ &\sim \sqrt{\frac{n+2}{n}}\left(\frac{n+2}{2H_{n+2}}\frac{D_s}{D_{ls}}\right)^{\frac{1}{n}}\theta_0^{\frac{n+1}{n}}.\end{aligned} \tag{5.73}$$

5.4.2 Magnifications and Images of the Relativistic Images

We will briefly review the magnifications $\mu_{N\geq 1}$ and the angles $\theta_{N\geq 1}$ of the relativistic images [72, 63] and investigate them in the Tangherlini spacetime. We use the deflection angle $\alpha(\theta)$ (5.32) in this subsection.

When the winding number $N \geq 1$, we define an angle $\theta^0_{N\geq 1}$ by

$$\alpha(\theta^0_{N\geq 1}) = 2\pi N. \tag{5.74}$$

From Eqs. (5.32) and (5.74), we obtain

$$\theta^0_{N\geq 1} = \frac{b_c}{D_l}\left[1 + e^{\left(\bar{b}-2\pi N\right)\sqrt{n}}\right]. \tag{5.75}$$

We expand the deflection angle $\alpha(\theta)$ around $\theta = \theta^0_{N\geq 1}$ to obtain the effective deflection angle $\bar{\alpha}$. We define a small angle

$$\Delta\theta_{N\geq 1} \equiv \theta_{N\geq 1}(\phi) - \theta^0_{N\geq 1}, \tag{5.76}$$

where $\theta_{N\geq 1}(\phi)$ is the solution of the lens equation (5.67) or the relativistic image angle with the winding number $N \geq 1$. From Eqs. (5.32) and (5.75), the effective deflection angle of the light in the strong field limit is given by

$$\bar{\alpha} = -\frac{D_l}{b_c}\frac{e^{\sqrt{n}\left(-\bar{b}+2\pi N\right)}}{\sqrt{n}}\Delta\theta_{N\geq 1}. \tag{5.77}$$

We substitute the effective deflection angle (5.77) into the lens equation (5.67) and obtain

$$\phi = \theta^0_{N\geq 1} + \left[1 + \frac{D_l}{b_c}\frac{D_{ls}}{D_s}\frac{e^{\sqrt{n}\left(-\bar{b}+2\pi N\right)}}{\sqrt{n}}\right]\Delta\theta_{N\geq 1}. \tag{5.78}$$

From Eqs. (5.76) and (5.78), We get the the relativistic image angle $\theta_{N\geq 1}(\phi)$

$$\theta_{N\geq 1}(\phi) \simeq \theta^0_{N\geq 1} + \frac{b_c}{D_l}\frac{D_s}{D_{ls}}\sqrt{n}e^{\sqrt{n}(\bar{b}-2\pi N)}\left(\phi - \theta^0_{N\geq 1}\right), \tag{5.79}$$

where we have used $b_c/D_l \ll 1$. From Eqs. (5.75) and (5.79), the innermost relativistic image angle is obtained by

$$\theta_\infty = \theta^0_\infty = \frac{b_c}{D_l}. \tag{5.80}$$

From Eqs. (5.75), (5.79) and (5.80), the difference of the angles between the outermost relativistic image and innermost one is given by

$$\theta_1 - \theta_\infty \simeq \theta^0_1 - \theta_\infty = \theta_\infty e^{\sqrt{n}(\bar{b}-2\pi)}. \tag{5.81}$$

The magnification $\mu_{N\geq 1}$ of the relativistic image is obtained by

$$\begin{aligned}\mu_{N\geq 1} &\simeq \frac{\theta_{N\geq 1}}{\phi}\left.\frac{d\theta_{N\geq 1}}{d\phi}\right|_{\theta_{N\geq 1}=\theta^0_{N\geq 1}} \\ &\simeq \frac{1}{\phi}\frac{b_c^2}{D_l^2}\frac{D_s}{D_{ls}}\sqrt{n}e^{\sqrt{n}(\bar{b}-2\pi N)}.\end{aligned} \tag{5.82}$$

The sum of the magnifications of all the relativistic images is given by

$$\begin{aligned}\sum_{N=1}^{\infty}\mu_N &\simeq \mu_1 \simeq \frac{1}{\phi}\frac{b_c^2}{D_l^2}\frac{D_s}{D_{ls}}\sqrt{n}e^{\sqrt{n}(\bar{b}-2\pi)} \\ &\simeq \frac{2}{H_{n+2}^{\frac{2}{n}}\sqrt{n}\phi}\left[\frac{(n+2)D_s}{2D_{ls}}\right]^{\frac{2}{n}+1}\theta_0^{\frac{2n+2}{n}}e^{\sqrt{n}(\bar{b}-2\pi)}.\end{aligned} \tag{5.83}$$

The sum of the magnification of all the relativistic images become unity when the source angle is

$$\phi \simeq \frac{2}{H_{n+2}^{\frac{2}{n}}\sqrt{n}}\left[\frac{(n+2)D_s}{2D_{ls}}\right]^{\frac{2}{n}+1}\theta_0^{\frac{2n+2}{n}}e^{\sqrt{n}(\bar{b}-2\pi)}. \tag{5.84}$$

In the directly aligned limit, the ratio of the magnification of the weak field image divided by the sum of the magnification of all the relativistic images is given by

$$\frac{\mu_0}{\sum_{N=1}^{\infty}\mu_N} \simeq \frac{\mu_0}{\mu_1} \simeq \frac{H_{n+2}^{\frac{2}{n}}\sqrt{n}}{n+1}\left[\frac{2D_{ls}}{(n+2)D_s\theta_0}\right]^{\frac{2}{n}+1}e^{\sqrt{n}(2\pi-\bar{b})}. \tag{5.85}$$

The ratio shows that the relativistic images are always fainter than images in the weak field. Thus, we can ignore the effect of the relativistic images on the light curve. However, this does not mean that we cannot observe the relativistic images since they can get bright when the source angle is small.

The sum of the magnifications of the relativistic images excluding the outermost relativistic image is given by

$$\sum_{N=2}^{\infty}\mu_N \simeq \mu_2 \simeq \frac{1}{\phi}\frac{b_c^2}{D_l^2}\frac{D_s}{D_{ls}}\sqrt{n}e^{\sqrt{n}(\bar{b}-4\pi)}. \tag{5.86}$$

From Eqs. (5.86) and (5.82), the ratio of the magnification of the outermost relativistic image divided by the sum of the magnification of the other relativistic images is given by

$$\frac{\mu_1}{\sum_{N=2}^{\infty}\mu_N} \simeq \frac{\mu_1}{\mu_2} \simeq e^{\sqrt{n}2\pi}. \tag{5.87}$$

5.5 Summary of this chapter

We investigated the gravitational lensing effects in the Tangherlini spacetime in the weak gravitational field and in the strong field limit. The Tangherlini lens would be work as a wide-range toy model for a exotic lens model or a general spherical lens model [21, 36, 44, 76] with a photon sphere. The gravitational lensing in the strong field limit in higher dimension would be related to the nature of the higher dimensional black hole such as quasi-normal modes of black hole [68, 69] and high-energy absorption cross section [70].

We derived the divergent part of the deflection angle in all dimensions and the regular part in 4, 5 and 7 dimensions in the strong field limit, the deflection angle in all dimensions under the weak gravitational approximation and the relation between the size of the Einstein ring and the ones of the relativistic Einstein rings in all dimensions. We also shown that the relativistic images are always fainter than the images in the weak gravitational field.

Kitamura *et al.* [36] studied the demagnification of the light curves of the exotic lens object in the weak gravitational field. We conclude that the images in the strong gravitational field have little effect on the total light curve and that the characteristic demagnification of the light curve will appear after considering the images in the strong gravitational field for $n > 1$.

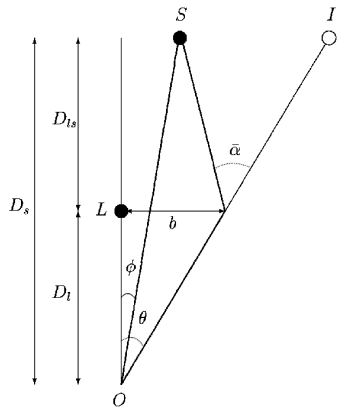

Figure 5.1: The configuration of the gravitational lensing. The light ray emitted by the source object S bends on the lens plane and the observer O does not observe the source S with the source angle ϕ but the image I with the image angle θ. $\bar{\alpha}$ is the effective deflection angle and b is the impact parameter of the light. D_l and D_{ls} are the distances between the observer O and the lens object L and between the lens object L and the source object S, respectively. The distance between the observer O and the source S is given by $D_s = D_l + D_{ls}$. [22]

Chapter 6

Conclusion

We examined a gravitational lens model inspired by modified gravity theories, exotic matter and energy. By using an asymptotically flat, static and spherically symmetric spacetime model of which metric depends on the inverse distance to the power of positive n. In Chapter2, it was shown in the weak field and thin lens approximations that demagnifying gravitational lenses could appear, provided the impact parameter of light $\hat{\beta}$ and the power n satisfy $\hat{\beta} > 2/(n+1)$ in the units of the Einstein ring radius under a large n approximation.

Therefore, time-symmetric demagnification parts in numerical light curves by gravitational microlensing (Abe, Astrophys. J. 725, 787, 2010) may be an evidence of an Ellis wormhole but they do not always prove it. Such a gravitational demagnification of the light might be used for hunting a clue of exotic matter and energy that are described by an equation of state more general than the Ellis wormhole case. Examples of $n = 3$ and 10 show maximally ~ 10 and ~ 60 percent depletion of the light, when the source position is $\hat{\beta} \sim 1.1$ and $\hat{\beta} \sim 0.7$, respectively. It is left as a future work to perform a numerical campaign for the vast parameter space. The gravitational demagnification of light occurs, presumably because modified lenses could act as an effectively negative (quasi-local) mass on a particular light ray (through the Ricci focusing). Regarding this issue, a more rigorous formulation is needed. It would be interesting to study a relation between the model parameter n and vital modified gravity theories (or matter models with an exotic equation of state) and also to make an interpretation of the parameter n in the framework of the theory of general relativity.

The analytical approximate solution in this paper is obtained at the linear order of $1/\hat{\beta}$ to discuss the total magnification. Tsukamoto and Harada [21] have studied the next order of $1/\hat{\beta}$ to discuss the signed magnification sums, namely the difference between the amplifications of two images.

In the Chapter 3 it was shown in the weak field and thin lens approximations that images due to lens models for the gravitational pull on light rays are tangentially elongated, whereas those by the other models for the gravitational repulsion on light rays are always radially distorted.

As a cosmological implication, it is suggested that cosmic voids might correspond to a $\kappa < 0$ and $\varepsilon < 0$ case and hence they could produce radially elongated images rather than tangential ones. It would be interesting to investigate numerically light propagation through realistic voids in cosmological simulations, because the present model obeys a simple power-law.

Furthermore, in Chapter 4 it was shown in the weak field and thin lens approximations that, for large n cases in the convex-type models, the centroid shift from the source position might move on a multiply-connected curve like a bow tie, while it is known to move on an ellipse for $n = 1$ case and to move on an oval curve for $n = 2$. This bow-tie shape by the convex-type exotic lens models is distinguishable from standard ones due to binary motions or due the microlensing by Schwarzschild lens. The distinctive feature such as the bow-tie shape may be used for searching (or constraining) localized exotic matter or energy with astrometric observations.

The parameter range relevant for the current and near-future missions such as Gaia and JASMIME is $10^{-11} < |\bar{\varepsilon}|/R_E^n < 10^{-7}$, where we assume that the accuracy in astrometry will reach a few micro arcseconds and the mission lifetime will be several years.

It was shown also that the centroid shift trajectory for concave-type repulsive models might be elongated vertically to the source motion direction like a prolate spheroid, whereas that for convex-type attractive models such as the Schwarzschild one is tangentially elongated like an oblate spheroid. The image centroid shift by the repulsive models is always negative, because the effective force is repulsive. For unseen lens objects, the negative shift can be hardly distinguished from the positive one. In this sense, it might be relatively difficult to investigate the repulsive models in astrometry.

Finally, in Chapter 5 we investigated the gravitational lensing effects in the Tangherlini spacetime in the weak gravitational field and in the strong field limit. The Tangherlini lens would be work as a wide-range toy model for a exotic lens model or a general spherical lens model [21, 36, 44, 76] with a photon sphere. The gravitational lensing in the strong field limit in higher dimension would be related to the nature of the higher dimensional black hole such as quasi-normal modes of black hole [68, 69] and high-energy absorption cross section [70].

We derived the divergent part of the deflection angle in all dimensions and the regular part in 4, 5 and 7 dimensions in the strong field limit, the deflection angle in all dimensions under the weak gravitational approxima-

tion and the relation between the size of the Einstein ring and the ones of the relativistic Einstein rings in all dimensions. We also shown that the relativistic images are always fainter than the images in the weak gravitational field.

Kitamura *et al.* [36] studied the demagnification of the light curves of the exotic lens object in the weak gravitational field. We conclude that the images in the strong gravitational field have little effect on the total light curve and that the characteristic demagnification of the light curve will appear after considering the images in the strong gravitational field for $n > 1$.

Bibliography

[1] S. Frittelli, T. P. Kling, and E. T. Newman, Phys. Rev. D **61**, 064021 (2000).

[2] K. S. Virbhadra, and G. F. R. Ellis, Phys. Rev. D **62**, 084003 (2000).

[3] K. S. Virbhadra, and G. F. R. Ellis, Phys. Rev. D **65**, 103004 (2002).

[4] K. S. Virbhadra, Phys. Rev. D **79**, 083004 (2009).

[5] K. S. Virbhadra, and C. R. Keeton, Phys. Rev. D **77**, 124014 (2008).

[6] K. S. Virbhadra, D. Narasimha, and S. M. Chitre, Astron. Astrophys. **337**, 1 (1998).

[7] J. P. DeAndrea, and K. M. Alexander, ArXiv:1402.5630 [gr-qc].

[8] E. F. Eiroa, G. E. Romero, and D. F. Torres, Phys. Rev. D **66**, 024010 (2002).

[9] V. Perlick, Phys. Rev. D **69**, 064017 (2004).

[10] H. G. Ellis, J. Math. Phys. **14**, 104 (1973).

[11] M. S. Morris, and K. S. Thorne, Am. J. Phys. **56**, 395 (1988).

[12] M. S. Morris, K. S. Thorne, and U. Yurtsever, Phys. Rev. Lett. **61**, 1446 (1988).

[13] L. Chetouani, and G. Clément, Gen. Relativ. Gravit. **16**, 111 (1984).

[14] G. Clément, Int. J. Theor. Phys. 23, 335 (1984).

[15] M. Safonova, D. F. Torres, and G. E. Romero, Phys. Rev. D **65**, 023001 (2001).

[16] A. A. Shatskii, Astron. Rep. **48**, 525 (2004).

[17] K. K. Nandi, Y. Z. Zhang, and A. V. Zakharov, Phys. Rev. D **74**, 024020 (2006).

[18] F. Abe, Astrophys. J. **725**, 787 (2010).

[19] Y. Toki, T. Kitamura, H. Asada, and F. Abe, Astrophys. J. **740**, 121 (2011).

[20] N. Tsukamoto, T. Harada, K. Yajima, Phys. Rev. D **86**, 104062 (2012).

[21] N. Tsukamoto, and T. Harada, Phys. Rev. D **87**, 024024 (2013).

[22] N. Tsukamoto, T. Kitamura, K. Nakajima, and H. Asada, Phys. Rev. D **90**, 064043 (2014)

[23] C. M. Yoo, T. Harada, and N. Tsukamoto, Phys. Rev. D **87**, 084045 (2013).

[24] T. K. Dey, and S. Sen, Mod. Phys. Lett. A, **23**, 953 (2008).

[25] A. Bhattacharya, and A. A. Potapov, Mod. Phys. Lett. A, **25**, 2399 (2010).

[26] K. Nakajima, and H. Asada, Phys. Rev. D **85**, 107501 (2012).

[27] G. W. Gibbons and M. Vyska, Class. Quant. Grav. **29** 065016 (2012).

[28] M. Visser, *Lorentzuan Wormholes: From Einstein to Hawking* (AIP, NY, 1995).

[29] S. Capozziello, V. F. Cardone, and A. Troisi, Phys. Rev. D **73**, 104019 (2006).

[30] Z. Horvath, L. A. Gergely, D. Hobill, S. Capozziello, M. De Laurentis, arXiv:1207.1823.

[31] S. Mendoza, T. Bernal, X. Hernandez, J. C. Hidalgo, L. A. Torres, arXiv:1208.6241.

[32] H. Asada, Prog. Theor. Phys. **125**, 403 (2011).

[33] P. Schneider, J. Ehlers, E. E. Falco, *Gravitational Lenses* (Springer, NY, 1992).

[34] Z. Horvath, L. Gergely, and D. Hobill, Class. Quant. Grav. **27**, 235006 (2010).

[35] N. Dadhich, R. Maartens, P. Papadopoulos, and V. Rezania, Phys. Lett. B, **487**, 1 (2000).

[36] T. Kitamura, K. Nakajima, and H. Asada, Phys. Rev. D **87**, 027501 (2013).

[37] R. Takahashi, and H. Asada, Astrophys. J. **768**, L16 (2013).

[38] H. Bondi, Rev. Mod. Phys. **29**, 423 (1957).

[39] M. Jammer, *Concepts of Mass in Classical and Modern Physics*, (Harvard University Press, Cambridge, MA, 1961)

[40] M. Jammer, *Concepts of Mass in Contemporary Physics and Philosophy*, (Princeton University Press, Princeton, NJ, 1999)

[41] J. G. Cramer, R. L. Forward, M. S. Morris, M. Visser, G. Benford, and G. A. Landis, Phys. Rev. D **51**, 3117 (1995).

[42] T. Piran, Gen. Relativ. Gravit. **29**, 1363 (1997).

[43] G. Gibbons, and H. Kodama, Prog. Theor. Phys. **121**, 1361 (2009).

[44] K. Izumi, C. Hagiwara, K. Nakajima, T. Kitamura, and H. Asada, Phys. Rev. D **88**, 024049 (2013).

[45] M. A. Walker, Astrophys. J. **453**, 37 (1995).

[46] M. Miyamoto, and Y. Yoshii, Astron. J. **110**, 1427 (1995).

[47] M. Hosokawa, K. Ohnishi, and T. Fukushima, Astron. J. **114**, 1508 (1997).

[48] N. Safizadeh, N. Dalal, and K. Griest, Astrophys. J. **522**, 512 (1999).

[49] Y. Jeong, C. Han, and S. Park, Astrophys. J. **511**, 569 (1999).

[50] G. F. Lewis, X. R. Wang, Prog. Theor. Phys. **105**, 893 (2001).

[51] H. Asada, Astrophys. J. **573**, 825 (2002).

[52] C. Han, and C. Lee, Mon. Not. Roy. Astron. Soc. **329**, 163 (2002).

[53] C. Claudel, K. S. Virbhadra, and G. F. R. Ellis, J. Math. Phys. **42**, 818 (2001).

[54] V. Perlick, Living Rev. Relativity **7**, 9 (2004), http://relativity.livingreviews.org/Articles/lrr-2004-9.

[55] V. Perlick, arXiv:1010.3416[gr-qc].

[56] A. O. Petters, H. Levine and J. Wambsganss, *Singularity Theory and Gravitational Lensing* (Birkhauser, Boston, 2001).

[57] P. Schneider, C. S. Kochanek and J. Wambsganss, *Gravitational Lensing: Strong, Weak and Micro, Lecture Notes of the 33rd Saas-Fee Advanced Course*, edited by G. Meylan, P. Jetzer and P. North (Springer-Verlag, Berlin, 2006).

[58] M. Bartelmann, Class. Quant. Grav. **27**, 233001 (2010).

[59] J. Wambsganss, Living Rev. Relativity **1**, 12 (1998), http://www.livingreviews.org/Articles/Volume1/1998-12wamb/.

[60] S. W. Kim and Y. M. Cho, in *Evolution of the Universe and its Observational Quest* (Universal Academy Press, Tokyo, 1994), p. 353.

[61] C. Darwin, Proc. R. Soc. Lond. A **249** (1959).

[62] C. Darwin, Proc. R. Soc. Lond. A **263** (1961).

[63] V. Bozza, Phys. Rev. D **66**, 103001 (2002).

[64] W. Hasse and V. Perlick Gen. Relativ. Gravit. **34**, 415 (2002).

[65] V. Bozza, Gen. Relativ. Gravit. **42**, 2269 (2010).

[66] V. Bozza and L. Mancini, Astrophys. J. **753**, 56 (2012).

[67] F. R. Tangherlini, Nuovo Cim. **27**, 636 (1963).

[68] I. Z. .Stefanov, S. S. Yazadjiev and G. G. Gyulchev, Phys. Rev. Lett. **104**, 251103 (2010).

[69] S. -W. Wei and Y. -X. Liu, arXiv:1309.6375 [gr-qc].

[70] S. -W. Wei, Y. -X. Liu and H. Guo, Phys. Rev. D **84**, 041501 (2011).

[71] C. R. Keeton and A. O. Petters Phys. Rev. D **73**, 104032 (2006).

[72] V. Bozza, S. Capozziello, G. Iovane and G. Scarpetta, Gen. Relativ. Gravit. **33**, 1535 (2001).

[73] Refsdal, S. 1964, MNRAS, 128, 295

[74] Liebes, S. 1964, Phys. Rev., 133, 835

[75] Paczyński, B. 1986, Astrophys. J, 304, 1

[76] T. Kitamura, K. Izumi, K. Nakajima, C. Hagiwara and H. Asada, Phys. Rev. D **89**, 084020 (2014)

[77] Udalski A., et al., 1993, AcA **43**, 289

[78] Alcock, C., et al. 1993, Nature, **365**, 621

[79] Alcock, C., et al. 1995, Astrophys. J, **454**, L125

[80] Alcock, C., et al. 2000, Astrophys. J, **542**, 281

[81] Alcock, C., et al. 2001, Astrophys. J, **550**, L169

[82] Aubourg, E. et al. 1993, Nature, **365**, 623

[83] Einstein, A. 1936, Science **84**, 506

[84] Beaulieu J.-P., et al. 2006, Nature, **439**, 437

[85] Bond, I. A. 2004, Astrophys. J, **606**, L155

[86] Calchi Novati, S., Mancini, L., Scarpetta, G., & Wyrzykowski, Ł. 2009, MNRAS, **400**, 1625

[87] Bennett, D. P. et al. 2002, Astrophys. J, **579**, 639

[88] Wyrzykowski, Ł. et al. 2009, MNRAS, **397**, 1228

[89] Tisserand, P., et al. 2007, A & A, **469** 387

[90] Poindexter, S., et al., 2005, Astrophys. J, **633**, 914

[91] Gould, A. et al. 2009, Astrophys. J, **698**, L147

[92] Here, we mention the truncated expression in Eq. (2.1). Let us begin with considering a sphere whose radius from the center is denoted as r. The mass inside the sphere is denoted as $M(r)$. Any physically reasonable theory of gravity must admit the Newtonian limit, in accordance with experiments and observations. Hence, the metric components g_{tt} and g_{rr} in the weak field region are expected to have the Newton-type potential written as $M(r)/r$. Note that the part of $1/r$ comes from the

Green function for the Laplacian operator (and thus the Poisson equation). The fraction as $M(r)/r$ becomes the inverse distance only for a point mass case, while it is a more general function of the distance for extended objects. Roughly speaking, therefore, the ansatz of the spacetime metric Eq. (2.1) might correspond to assuming $M(r)$ in the power law of r. For example, $n = 0$, $n = 1$ and $n = 2$ correspond to isothermal spheres (as a simple model of a galaxy), the vacuum region outside of an bounded mass distribution, and Ellis worm holes, respectively. Ellis worm holes are non-vacuum and non-singular (regular) in the sense that they are associated with a particular scalar field configuration. Models under study thus describe a regular distribution of matter for $n \neq 1$.

[93] This shortcut is not widely known. Ref. [33] does not mention this and does explicit calculations of the off-diagonal terms in the Jacobian matrix (in section 8.1 of the book).

[94] JASMINE. http://www.jasmine-galaxy.org/index-ja.html

[95] Gaia. http://www.cosmos.esa.int/web/gaia/home